TABLE OF CONTENTS

I.	INTRODUCTION	1	1/A10
II.	THUNDERSTORM GUST FRONT	3	1/A12
	Review of Model	3	1/A12
	Physical Scaling	3	1/A12
	Sensitivity to Dimentionless Parameters	6	1/B1
	Pressure Distributions	33	1/C14
	Conditions Leading to Most Severe Wind Shear	33	1/C14
III.	WARM FRONT	37	1/D4
	Scaling Relationships	37	1/D4
	Simulation Results	39	1/D6
IV.	SUMMARY AND RECOMMENDATIONS	48	1/E1
V.	REFERENCES	49	1/E2
	APPENDIX A: Turbulent Transport Model of a Thunderstorm Gust Front	51	1/E4

NAS1.26:3002

COMPLETED

ORIGINAL

NASA Contractor Report 3002

Turbulent Transport Model of Wind Shear in Thunderstorm Gust Fronts and Warm Fronts

W. S. Lewellen, M. E. Teske, and H. Segur

CONTRACT NAS8-32037
MAY 1978

NASA

68

NASI.26:3002

NASA Contractor Report 3002

Turbulent Transport Model of Wind Shear in Thunderstorm Gust Fronts and Warm Fronts

W. S. Lewellen, M. E. Teske, and H. Segur
Aeronautical Research Associates of Princeton, Inc.
Princeton, New Jersey

Prepared for
George C. Marshall Space Flight Center
under Contract NAS8-32037

National Aeronautics
and Space Administration

**Scientific and Technical
Information Office**

1978

FOREWORD

The motivation for the research reported in this document was to simulate the low-level wind and turbulence profiles associated with both local thunderstorm gust fronts and synoptic-scale warm fronts using the Aeronautical Research Associates of Princeton, Inc. (A.R.A.P.) model of turbulent flow in the atmospheric boundary layer. The sensitivity of the thunderstorm gust front to five dimensionless parameters is examined as well as the sensitivity of the warm front to variations in the Rossby number. Conclusions resulted from the study relative to conditions which lead to wind shears hazardous for aircraft operations.

This research was conducted by Aeronautical Research Associates of Princeton for the National Aeronautics and Space Administration, George C. Marshall Space Flight Center, Huntsville, Alabama, under the technical direction of Mr. Dennis W. Camp and Mrs. Margaret B. Alexander of the Space Sciences Laboratory. The support for this work was provided by Mr. John Enders of the Aeronautical Operating Systems Division, Office of Advanced Research and Technology, NASA Headquarters.

NOMENCLATURE

C_a	ambient horizontal convergence surrounding the thunderstorm downdraft
f	Coriolis function $\sec^{-1}$
g	gravitational constant
h	height of computational domain; also height at which downdraft is released
M	Margules' parameter for the slope of a front $(\Delta u_g f T_o / g \Delta\theta)$
p	pressure
q	total turbulent velocity fluctuation
r	radial coordinate
Ro	Rossby number $(u_g / f z_o)$
T_o	reference temperature taken as 300°K in the simulations
U	mean radial velocity for the gust front, or mean horizontal velocity parallel to the warm front
u_g	geostrophic velocity parallel to the warm front
V	mean horizontal velocity normal to the warm front
v_g	geostrophic velocity normal to the warm front
W	mean vertical velocity
$\hat{w}$	characteristic velocity in the downdraft $(g\lvert\Delta\theta\rvert h / T_o)^{\frac{1}{2}}$
z	vertical coordinate
Δu_g	change in u_g across the warm front
$\Delta\theta$	change in θ across the warm front, or defect in θ within the downdraft.
η	component of vorticity
ψ	stream function
Γ_a	ambient potential temperature lapse rate
Λ	macroscale of turbulence
ρ	density
θ	virtual potential temperature
σ	spread of imposed downdraft at the top of the domain

Contour notation for the figures:

All contours except in Figs. 25-28 are labeled as a multiple of the normalizing value.

Contour notations for the figures (continued)

Velocities in Figs. 2-24 are normalized by $\hat{w}$, which for $\Delta\theta = -10°K$ and $h = 1.6$ km is equal to 22.87 m/sec. Dimensional times and length scales shown are for these particular values of $\Delta\theta$ and h. In Fig. 20 where $\hat{w} = 0$, velocities are still normalized by 22.87 m/sec for ready comparison with the other figures.

Velocities in Figs. 29-36 are normalized by Δu or the maximum value indicated in the figure title.

Temperatures in all figures are normalized by the appropriate $\Delta\theta$.

Pressure perturbations in Figs. 25-28 are given directly in millibars for $\Delta\theta = -10°K$ and $h = 1.6$ km. For other values Δp should be scaled by $(g\Delta\theta h)$.

LIST OF FIGURES

Figure

1 The leading edge of a gust front as marked by dust (from Ref. 13).

2 Model simulation of the leading edge of a gust front when visualized in terms of temperature defect intensity.

3 Contours of constant horizontal velocity as a function of r and z for the base case at consecutive simulation times. For $\Delta\theta = -10^{\circ}K$ and $h = 1.6$ km, $\hat{w} \approx 22.9$ m/sec.

4 Contours of constant potential temperature as a function of r and z for the base case at consecutive simulation times.

5 Contours of constant vertical velocity as a function of r and z for the base case at consecutive simulation times. For $\Delta\theta = -10^{\circ}K$ and $h = 1.6$ km, $\hat{w} = 22.9$ m/sec.

6 Contours of constant total velocity variance as a function of r and z for the base case at consecutive simulation times.

7 Contours of constant horizontal velocity as a function of r and z at t = 350 secs and 1000 secs ($t\hat{w}/h = 5$ & 14.3) for $\sigma/h = 0.31$ and 0.0625.

8 Contours of constant potential temperature as a function of r and z at t = 350 secs and 1000 secs ($t\hat{w}/h = 5$ & 14.3) for $\sigma/h = 0.31$ and 0.0625.

9 Contours of constant vertical velocity as a function of r and z at t = 350 secs and 1000 secs ($t\hat{w}/h = 5$ & 14.3) for $\sigma/h = 0.31$ and 0.0625.

10 Contours of constant horizontal velocity as a function of r and z at t = 350 secs and 1000 secs for $z_o/h = 6.25 \times 10^{-5}$ and 6.25×10^{-6}.

11 Contours of constant total velocity variance as a function of r and z at t = 350 secs and 1000 secs for $z_o/h = 6.25 \times 10^{-5}$ and 6.25×10^{-6}.

12 Contours of constant horizontal velocity as a function of r and z at t = 350 secs and 1000 secs for $w_j/\hat{w} = 0.109$ and 0.875.

13 Contours of constant potential temperature as a function of r and z at t = 350 secs and 1000 secs for $w_j/\hat{w} = 0.109$ and 0.875.

14 Contours of constant horizontal velocity as a function of r and z at t = 350 secs and 1000 secs for $\Gamma_a h/\Delta\theta$ = 0.48 and -0.48.

15 Contours of constant potential temperature as a function of r and z at t = 350 secs and 1000 secs for $\Gamma_a h/\Delta$ = 0.48 and -0.48.

16 Contours of constant total velocity variance as a function of r and z at t = 350 secs and 1000 secs for $\Gamma_a h/\Delta\theta$ = 0.48 and -0.48.

17 Contours of constant horizontal velocity as a function of r and z at t = 350 secs and 1000 secs for $C_a h/\hat{w}$ = 0 and 0.08.

18 Contours of constant potential temperature as a function of r and z at t = 350 secs and 1000 secs for $C_a h/\hat{w}$ = 0 and 0.08.

19 Flow variables as a function of y and z at t = 1000 secs for the simulated planar downdraft; (a) horizontal velocity, (b) potential temperature, (c) vertical velocity, and (d) total velocity variance.

20 Contours of constant (a) horizontal velocity, (b) vertical velocity (c) total velocity variance for $w_j/\hat{w} = \infty$ at t = 500 secs.

21 Contours of constant horizontal velocity for the downdraft of Fig. 20 with evaporation at t = 200, 500, and 1000 secs.

22 Contours of constant potential temperature for the downdraft of Fig. 20 with evaporation at t = 200, 500 and 1000 secs.

23 Contours of constant vertical velocity for the downdraft of Fig. 20 with evaporation at t = 200, 500 and 1000 secs.

24 Contours of constant total velocity variance for the downdraft of Fig. 20 with evaporation at t = 200, 500 and 1000 secs.

25 Contours of constant pressure perturbations for the base case at consecutive simulation times. Δp given in millibars for $\Delta\theta$ = -10°K , h = 1.6 km .

26 Contours of constant pressure perturbations for σ/h = 0.31 at t = 350. (Δp in millibars for $\Delta\theta$ = -10°K , h = 1.6 km.)

27 Contours of constant pressure perturbations for w_j/w = 0.875 at t = 350. (p in millibars for = -10 K , h = 1.6 km.)

28 Contours of constant pressure perturbations for z_o/h = 6.25×10^{-6} at t = 350. (Δp in millibars for $\Delta\theta$ = -10°K , h = 1.6 km.)

29 Distribution of mean wind parallel to a warm front near the surface for $Ro = 10^8$. Contours normalized by the total Δu_g across the front.

30 Distribution of mean wind normal to a warm front near the surface for $Ro = 10^8$. Contours normalized by $V_{max} = 0.18\Delta u_g$.

31 Distribution of potential temperature through a warm front near the surface for $Ro = 10^8$. Contours normalized by $\Delta\theta$ across the front.

32 Distribution of the total velocity variance through a warm front near the surface for $Ro = 10^8$. Contours normalized by $q^2_{max} = 0.0056(\Delta u_g)^2$.

33 Distribution of mean wind parallel to a warm front near the surface for $Ro = 10^6$. Contours normalized by the total Δu_g across the front.

34 Distribution of mean wind normal to a warm front near the surface for $Ro = 10^6$. Contours normalized by $V_{max} = 0.18\Delta u_g$.

35 Distribution of potential temperature through a warm front near the surface for $Ro = 10^6$. Contours normalized by $\Delta\theta$ across the front.

36 Distribution of the total velocity variance through a warm front near the surface for $Ro = 10^6$. Contours normalized by $q^2_{max} = 0.0056(\Delta u_g)$.

I. INTRODUCTION

The investigation of aircraft accidents as well as model simulation of wind distributions in the lowest 500 m of the atmosphere has shown that strong fronts are a major source of hazardous wind shear conditions (Refs. 1 and 2). In this report, we will simulate two types of hazardous front conditions. The first is the local gust front created by the rain-cooled outflow from a severe thunderstorm. The second is the synoptic-scale warm front with its stable temperature gradients leading to high wind shear at relatively low values of turbulence.

The numerical simulations described herein were performed using a computer model developed at A.R.A.P. over the last few years to solve for the velocity, temperature and turbulence distributions in the atmospheric boundary layer (Refs. 3-8). Details of our atmospheric boundary layer model, based on invariant modeling for the closure of the dynamic equations of the ensemble-averaged, single-point, second-order correlations of the fluctuating velocities and temperature, are given in Ref. 9. The basic assumption is that the third-order correlations of the velocity fluctuations depend upon the second-order correlations, the mean flow properties, and their derivatives in an invariant manner with respect to changes in flow geometry. This permits data from relatively simple flow experiments to be used in evaluating the necessary coefficients in the modeled terms.

Downdrafts from a thunderstorm have been a contributing factor in several specific aircraft accidents, e.g., at JFK Airport on June 24, 1975, and at Denver on August 7, 1975. These and other similar accidents have been considered case-by-case in Refs. 7-10. The present report uses the general gust front model to determine the sensitivity of the gust front structure to variations in the basic governing parameters. In this way, we determine what conditions lead to the most severe wind shear conditions below 500 m altitude.

The structure and evolution of the gust front as predicted by the A.R.A.P. model for nominal conditions has been presented at the 10th Conference on Severe Local Storms, October 18-21, 1977, Omaha, Nebraska. This paper is included herein as Appendix A. It includes a detailed listing of the equations used for the axisymmetric model simulation.

Several accidents have also been associated with warm fronts (Ref. 2). The warm front represents a stable balance between geostrophic and hydrostatic forces. The warm front simulations presented herein use the same basic model as the thunderstorm gust front with Coriolis forces added. The big difference in type and scale is accomplished by changes in the boundary conditions. While the thunderstorm gust front model follows the time evolution for typically 15-20 minutes simulation, a few hours are required for the development of the warm front. A review of the essential features

of the model as related to a warm front, its physical scaling, and simulation results are given in Section III.

II. THUNDERSTORM GUST FRONT

In this Section, we will first briefly review the model. Next, we will present the physical scaling of the phenomena in order to clarify the dimensionless parameters governing the flow. Third, we will present the results of several individual numerical simulations to exemplify the variation induced by different parameters. Finally, the results of the scaling and numerical simulations will be used to discuss the conditions which lead to the most severe wind shear conditions below 500 m altitude.

Review of Model

The simulated flowfield is illustrated in Fig. 1 of Appendix A. The downdraft may be simulated as either an axisymmetric or a plane cold jet impinging on the ground and spreading outward. It is driven by its negative buoyancy as represented by a defect in the potential temperature of the downdraft with respect to its surroundings. The complete equations are given in an axisymmetric coordinate system at the end of Appendix A. To obtain the equations in a two-dimensional, planar coordinate system, the radius r can be allowed to approach ∞. In this process, all of the variables with the wavy overbar should be multiplied by r, i.e., $r\tilde{\eta} = \eta$, $r\tilde{U} = U$, $r\tilde{uw} = \overline{uw}$, and $r\tilde{u\theta} = \overline{u\theta}$.

At the beginning of the simulation the cold shaft of air is released with some initial downward velocity at the top of the domain. The ground surface is represented by an effective aerodynamic roughness and a surface temperature. The ambient air status is represented by a lapse rate and the horizontal convergence induced by the parent thunderstorm.

As the downdraft impinges on the ground and spreads outward, it creates the local gust front. Under proper soil conditions, it picks up enough dust for the leading edge to be clearly visible as in Fig. 1. When the simulated front given in detail in Appendix A is visualized in terms of temperature defect intensity, with the vertical and horizontal dimensions shown to the same scale, the leading edge appears as shown in Fig. 2. The strong quantitative similarity between Figs. 1 and 2 is readily apparent. The quantitative predictions also appear consistent with available observations.

Physical Scaling

The dimensional variables affecting the downdraft are the potential temperature defect, $\Delta\theta$; the height, h, of the potential temperature defect; the surface roughness, z_o; the ambient lapse rate, Γ_a; the ambient convergence, $C_a = \partial W_a r/r\partial r$; and the vertical velocity W_j, and spread σ of the downdraft at the top of the domain. In forming the dimensionless variables, it is necessary to add one constant, the ratio of gravity, g, to the

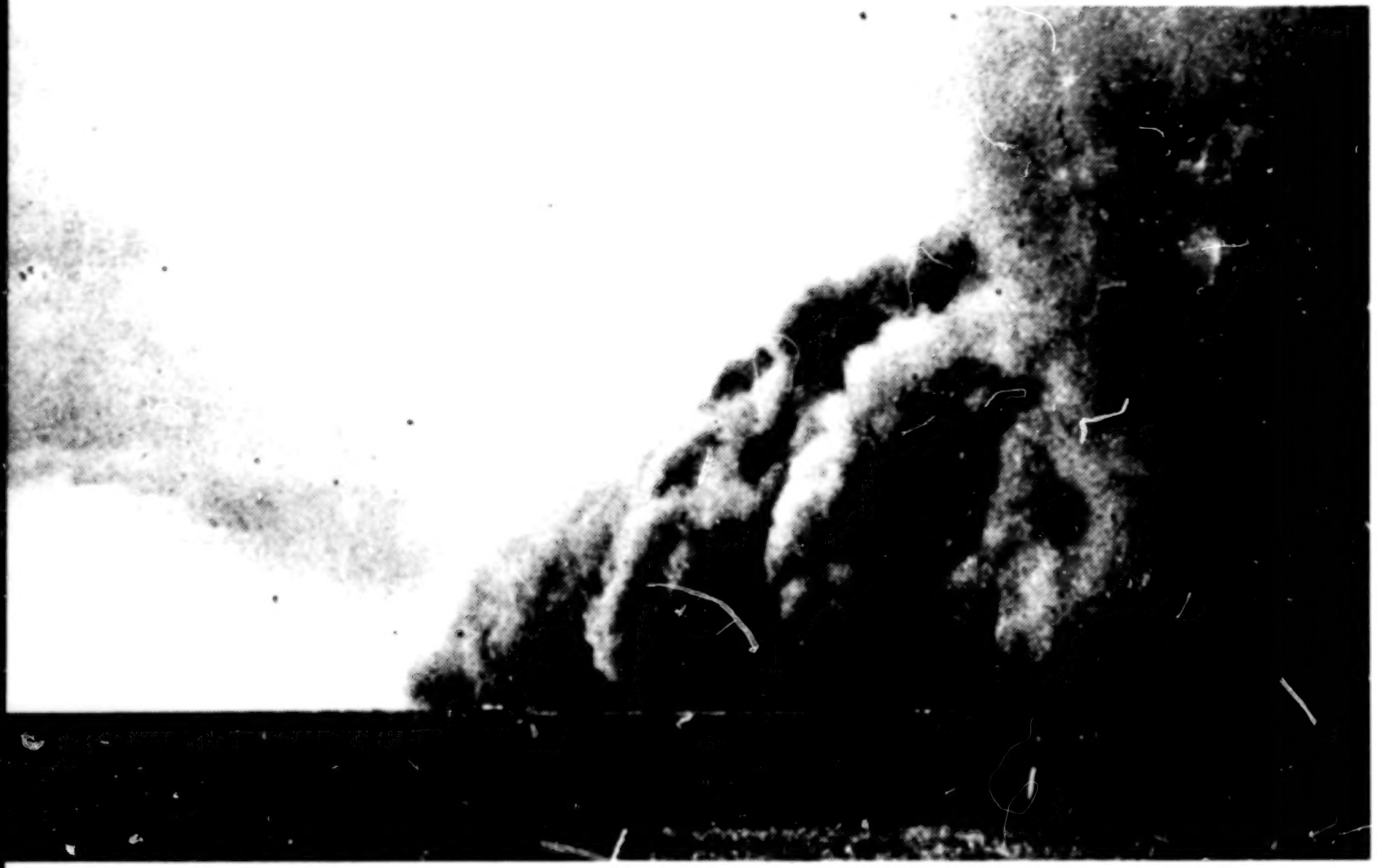

Figure 1. The leading edge of a gust front as marked by dust (from Ref. 13).

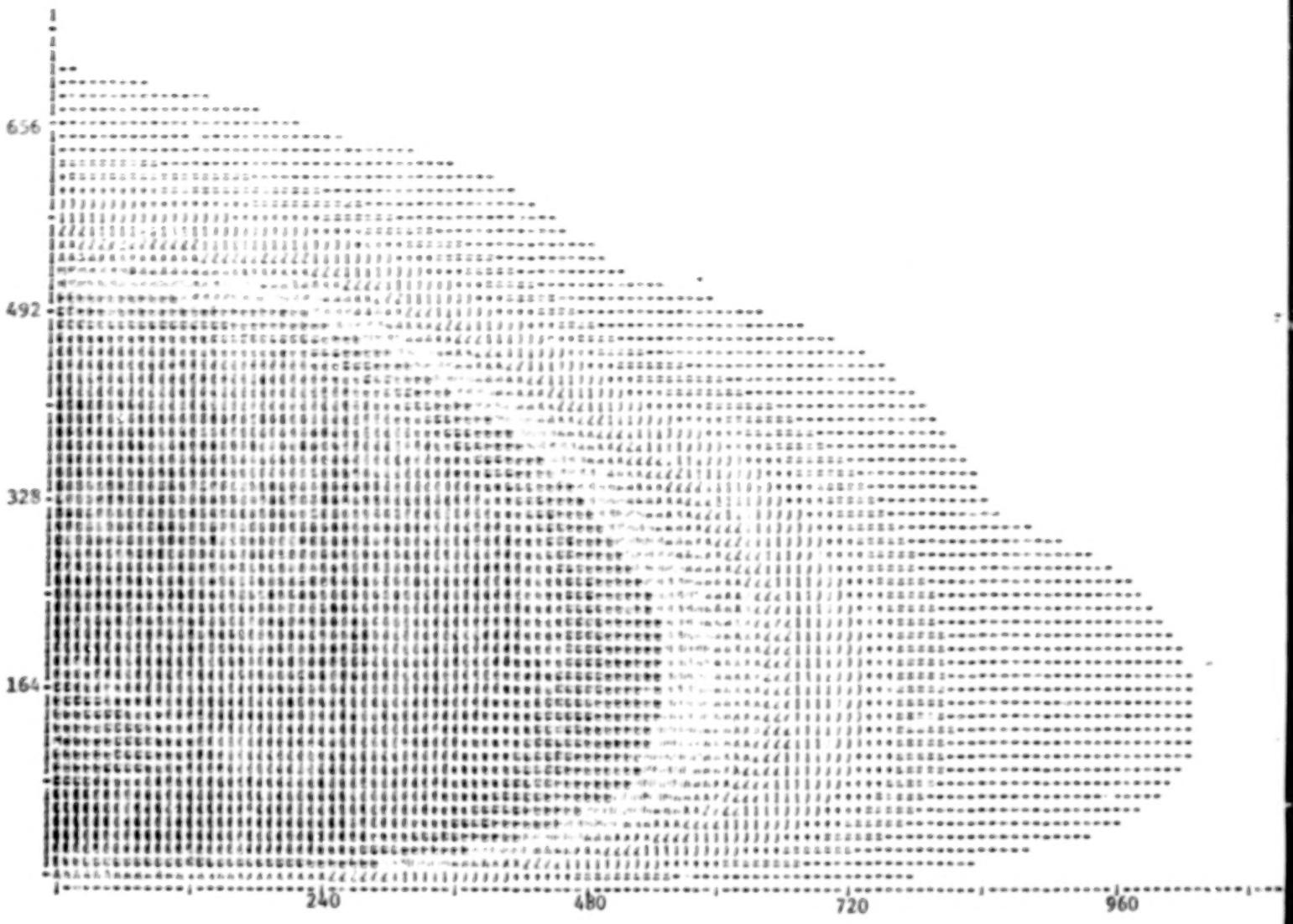

Figure 2. Model simulation of the leading edge of a gust front when visualized in terms of temperature defect intensity.

reference temperature T_o . When h is chosen as the characteristic length, $\Delta\theta$ the characteristic temperature and $(|\Delta\theta|hg/T_o)^{\frac{1}{2}} = \hat{w}$, the characteristic velocity; the flow may be specified in terms of the following five dimensionless parameters

$$w_j/\hat{w} \quad , \quad z_o/h \quad , \quad \Gamma_a h/\Delta\theta \quad , \quad C_a h/\hat{w} \quad , \quad \sigma/h \qquad (1)$$

The unsteady time evolution may then be viewed in terms of the dimensionless time $t\hat{w}/h$. Since the turbulence correlations are all being determined by the flow, they should all scale with $\hat{w}$ and $\Delta\theta$. There is the possibility of introducing another variable in association with the surface temperature. However, in the present model runs, the surface temperature has been set equal to the ambient air temperature at the surface.

The advantage of the above normalization is that the results of one model simulation can be used to determine the flow variables for other values of $\Delta\theta$ and h . The model simulation results given in Appendix A for $\Delta\theta = -10^{o}K$, $h = 1.6$ km , $\sigma = 2$ km , $z_o = 1$ m , $\Gamma_a = 0$, and $C_a = 5 \times 10^{-4}$ sec , have

$$\begin{aligned} w_j/\hat{w} &= 0.437 \\ z_o/h &= 6.25 \times 10^{-4} \\ \sigma/h &= 1.25 \\ \Gamma_a h/\Delta\theta &= 0 \\ C_a h/\hat{w} &= 0.04 \end{aligned} \qquad (2)$$

These results are valid for other values of $\Delta\theta$ and h as long as all velocities are scaled by $\hat{w}$, all lengths by h , and all temperatures by $\Delta\theta$. The only restriction is that the dimensionless parameter values given in Eq. (2) must be maintained. The dimensionless character of the gust front may be expected to vary as these governing parameters vary.

The evolution of U , θ , W and q^2 is shown in Figs. 3-6 for this typical model run. In these figures, we show only the bottom 500 m of the flow, since for aircraft operations this is the region of greatest concern.

In the next section, the results of a number of model simulation runs are given to elucidate the influence of varying the five dimensionless parameters.

Sensitivity to Dimensionless Parameters

In this section we present the results of eleven individual model simulations for different combinations of the dimensionless parameters given in Eq. (1). This by no means exhausts the possibilities, but it does provide a good indication of the variability to be expected. The nominal values of the parameters used in the

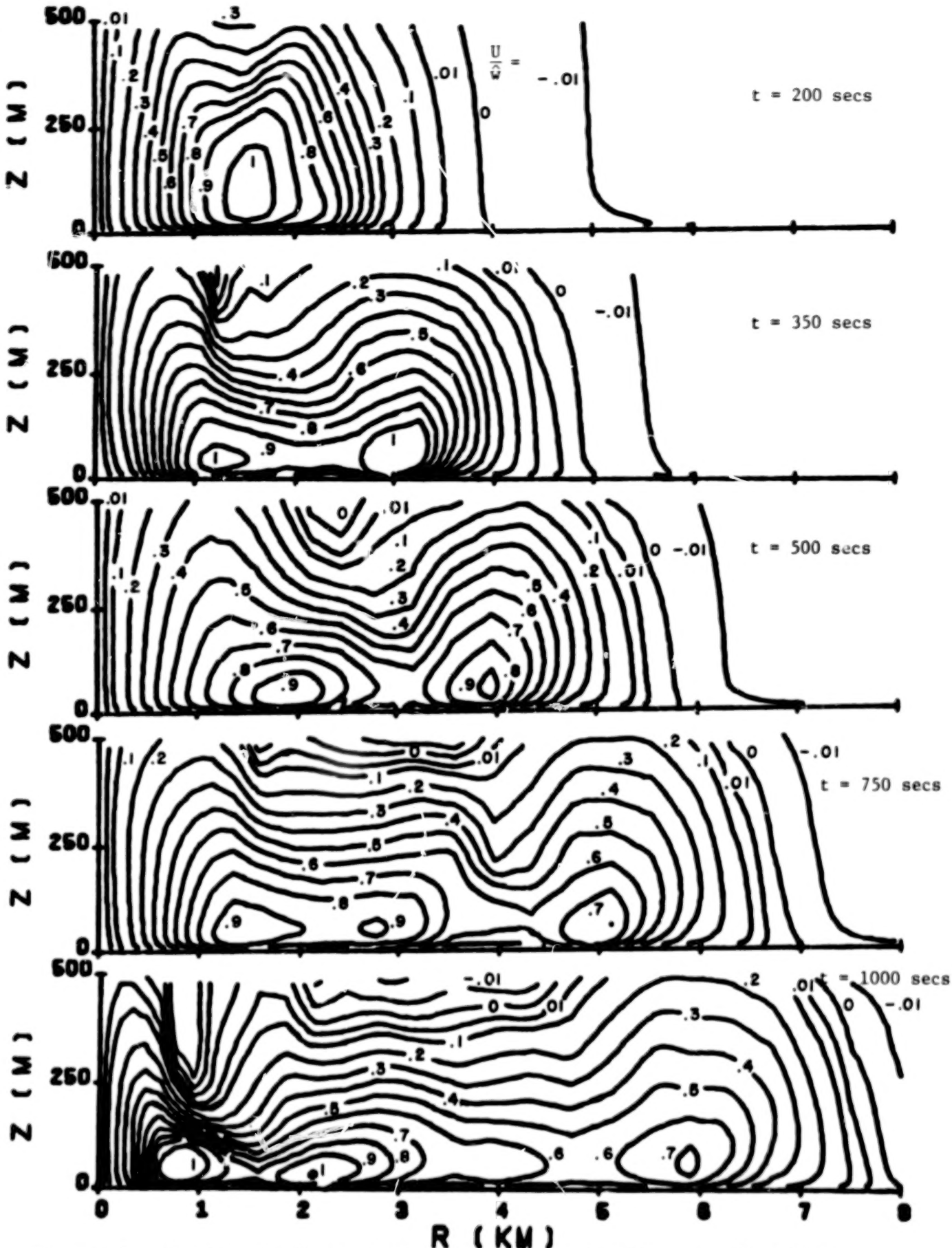

Figure 3. Contours of constant horizontal velocity as a function of r and z for the base case at consecutive simulation times. For $\Delta\theta = -10^{\circ}K$ and $h = 1.6$ km, $\hat{W} \approx 22.9$ m/sec .

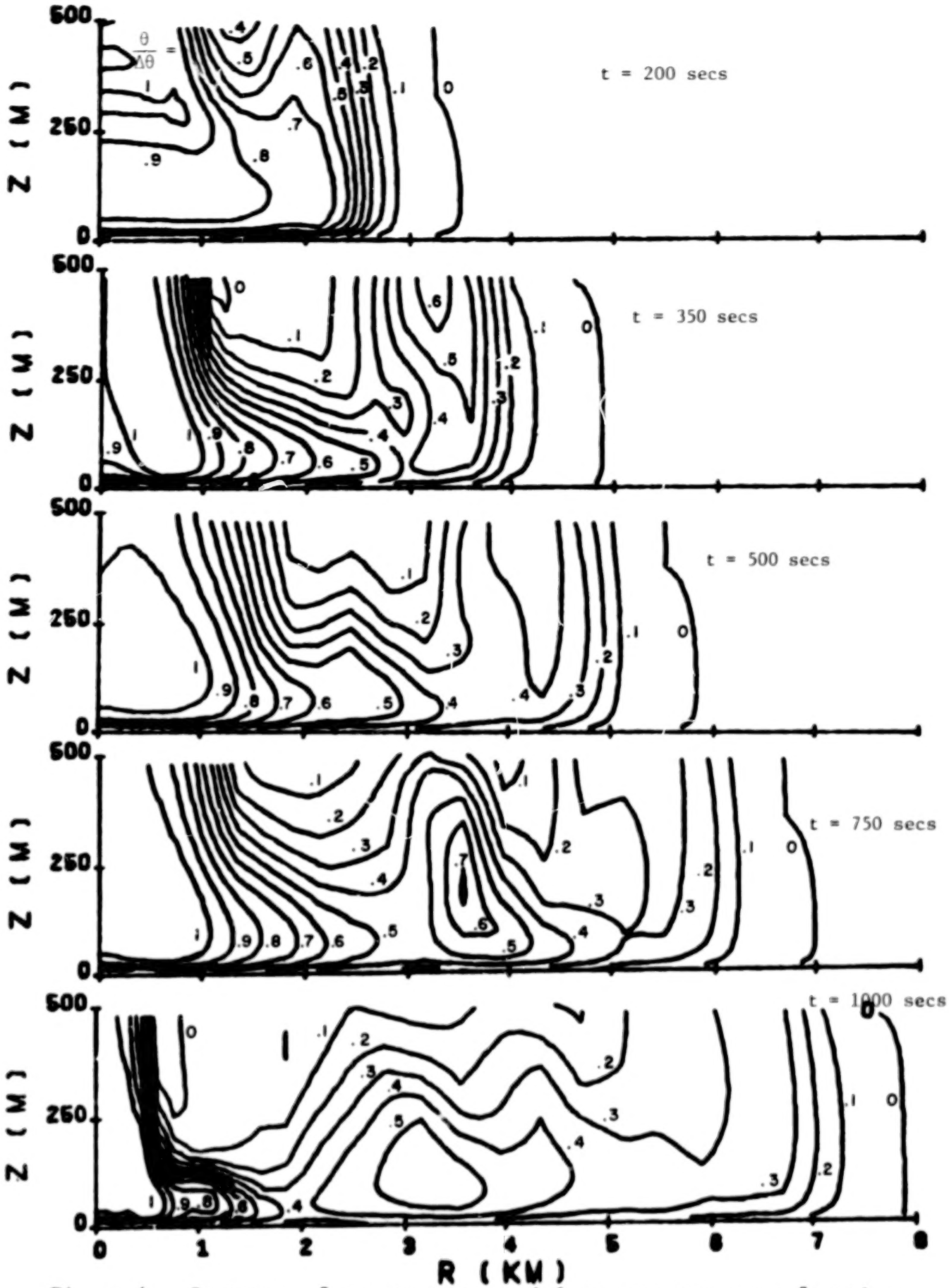

Figure 4. Contours of constant potential temperature as a function of r and z for the base case at consecutive simulation times.

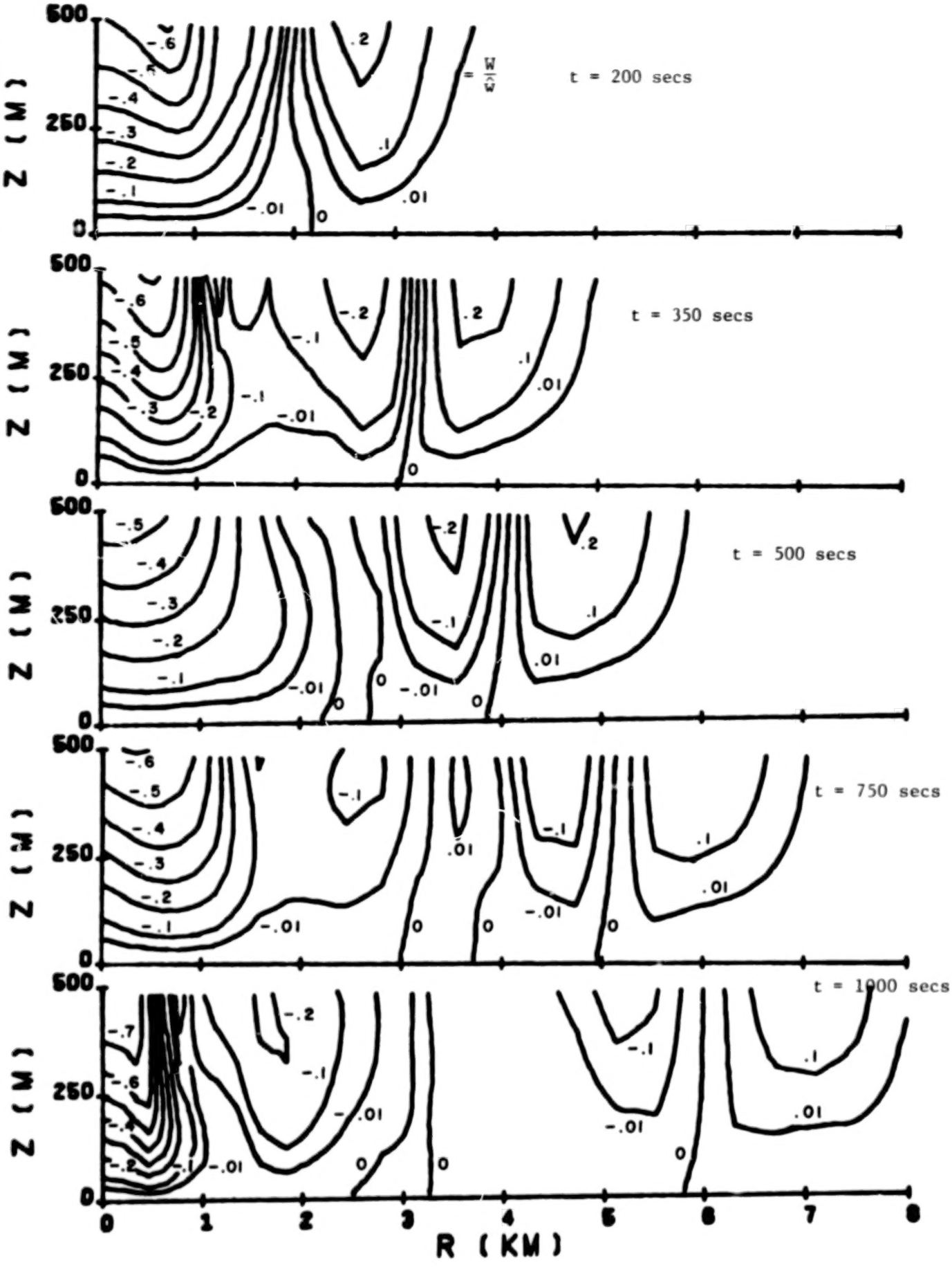

Figure 5. Contours of constant vertical velocity as a function of r and z for the base case at consecutive simulation times. For $\Delta\theta = -10^{\circ}K$ and $h = 1.6$ km, $\Phi = 22.9$ m/sec.

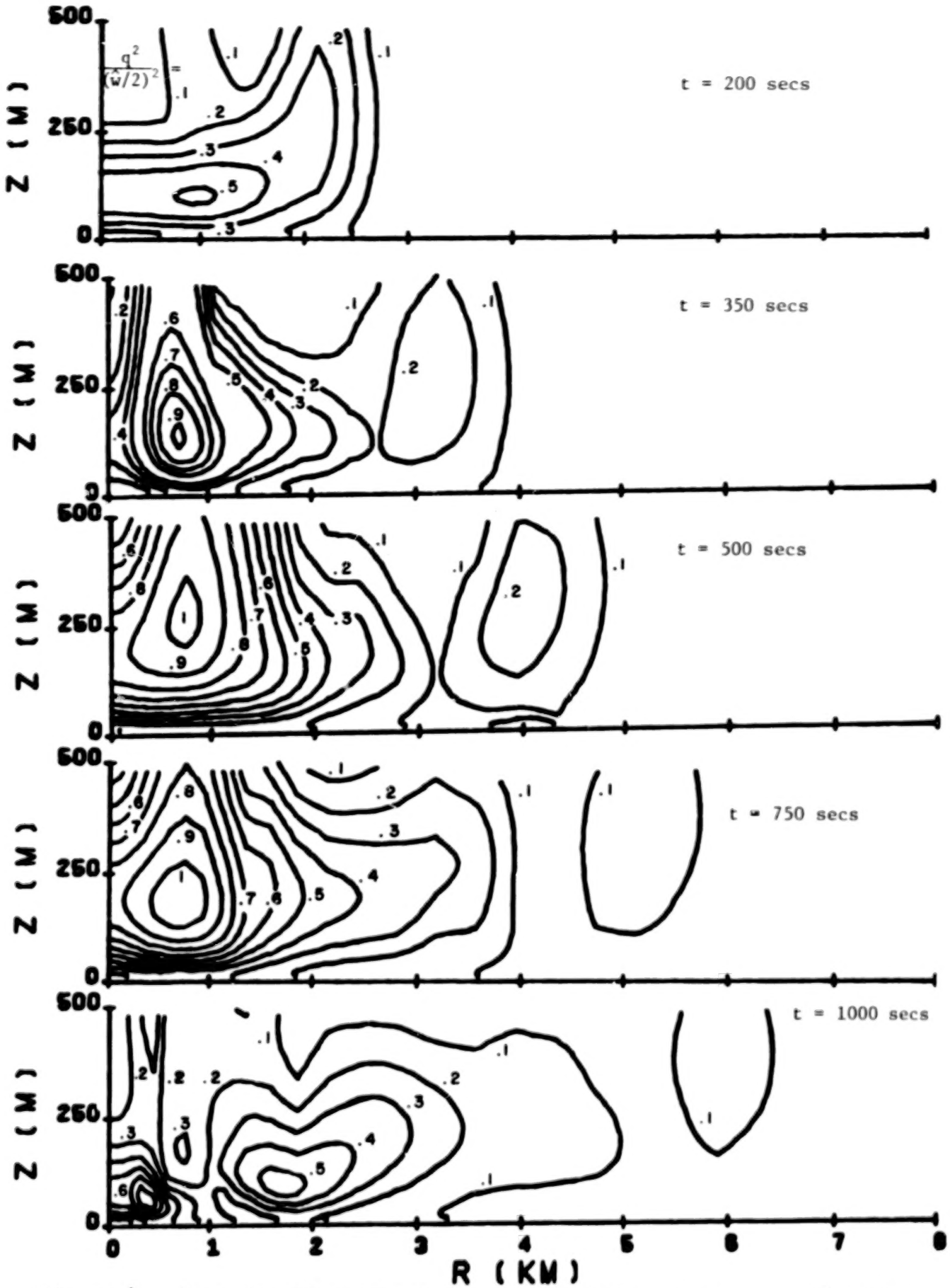

Figure 6. Contours of constant total velocity variance as a function of r and z for the base case at consecutive simulation times.

simulation in Appendix A and given in Eq. (2) are taken as the base values and each of the parameters allowed to vary in turn with the others held fixed. Table 1 summarizes the input parameter values, and gives a few key measures of the simulation output. Three simulations of a two-dimensional, planar downdraft are also included in Table 1.

A quick look at Table 1 shows that the phenomenon is quite similar throughout most of the range of the parameters considered. Within the axisymmetric cases, the parameter which induces most influence is σ/h. Too narrow a downdraft gets destroyed by turbulent mixing before it reaches the surface. Thus when $\sigma/h \leq 0.1$ the gust front does not get a chance for effective formation. At larger values of σ/h the maximum horizontal gust velocity is relatively independent of σ/h, but the depth of the outflow is increased as σ/h increases. Thus the larger σ/h, the slower the decrease in U as the gust spreads radially outward.

The sensitivity to σ/h may be seen in greater detail by comparing Figs. 7-9 with the corresponding curves in Figs. 3 and 4. The erosion of the temperature defect before it reaches the ground is clearly evident in Fig. 6a for the small value of $\sigma/h = 0.0625$.

The influence of z_o/h is seen by comparing Figs. 10 and 11 with the corresponding curves in Figs. 3 and 6. Increasing the roughness does increase the turbulence level modestly, but, even an increase of a factor of 100 does not raise the height at which the maximum horizontal velocity occurs as much as might be expected. At the simulation time of 1000 sec, the height of U_{max} in the outer region of the gust is only raised from $z \simeq 30$ m to $z \simeq 65$ m by increasing z_o by 100 times.

The influence of changing $w_j/\hat{w}$ may be seen by comparing Figs. 10 and 11 with Figs. 1 and 2. Increasing $w_j/\hat{w}$ has two effects. It increases U_{max} approximately by a factor of $(1 + w_j^2/\hat{w}^2)^{\frac{1}{2}}$ and it slightly increases the depth of the outflow layer.

The influence of changing the ambient stability as represented by the parameter $\Gamma_a h/\Delta\theta$ may be seen by comparing Figs. 14-16 with Figs. 3, 4 and 6. The major influence appears to be to increase the depth of the outflow layer in the unstable case with only a slight reduction in depth for the stable case. In the stable case, most of the influence of the change could be incorporated into the scaling by noting that the effective potential temperature defect is decreased. By keeping the defect the same at the top of the domain, the ambient stability forces it to be less at the surface.

The least influential parameter in these runs was the value of the ambient convergence, as may be seen from Figs. 17 and 18.

TABLE I

Gust Front Model Parameters

Simulation #	$\frac{w_j}{\hat{U}}$	$\frac{z_o}{h}$	$\frac{\sigma}{h}$	$\frac{\Gamma_a h}{\Delta\theta}$	$\frac{C_a h}{\hat{U}}$	$\frac{U_{max}}{\hat{U}}$	$\frac{q^2_{max}}{\hat{U}^2}$	$\frac{r}{h}$ ($@\ \frac{t\hat{U}}{h} = 1.43$)	$\frac{U_{max@5km}}{\hat{U}}$	$\frac{z_{2_{U_{max}}}}{}$
Axisymmetric simulations										
1	0.437	6.25×10^{-4}	1.25	0	0.04	1.3	.32	5	.78	.033
2	0.437	6.25×10^{-4}	0.31	0	0.04	1.1	.33	2.8	0	-
3	0.109	6.25×10^{-4}	1.25	0	0.04	1.0	.40	4.9	.48	.031
4	0.437	6.25×10^{-4}	0.0625	0	0.04	0.45	.22	1.6	0	-
5	0.437	6.25×10^{-5}	1.25	0	0.04	1.4	.32	5.2	.75	.042
6	0.437	6.25×10^{-4}	1.25	0	0	1.3	.24	5.4	.74	.061
7	0.875	6.25×10^{-4}	1.25	0	0.04	1.6	.19	5.4	.93	.086
8	0.437	6.25×10^{-6}	1.25	0	0.04	1.4	.32	5.4	.88	.028
9	0.437	6.25×10^{-4}	1.25	0	0.08	1.3	.31	4.4	.74	.035
10	0.437	6.25×10^{-4}	1.25	0.48	0.04	1.3	.71	5.5	.53	.087
11	0.437	6.25×10^{-4}	1.25	-0.48	0.04	1.5	.32	5.1	.83	.039
Planar 2-D simulations										
12	0.437	6.25×10^{-4}	1.25	0	0.04	1.1	.25	4.5*	.86	.083
13†	∞	6.25×10^{-4}	1.25	0	0.04	0.30	.022	2.2	0	-
14†	(same as 13 but with evaporation)					0.67	.20	4.0	.26	.05

* $@\ \frac{t\hat{U}}{h} = 11.7$

† These two runs have been normalized by the same value of $\hat{U} = 22.87$ m/sec as the others although it would be more appropriate to use $w_j = 10$ m/sec for #13 and 17.1 m/sec for #14.

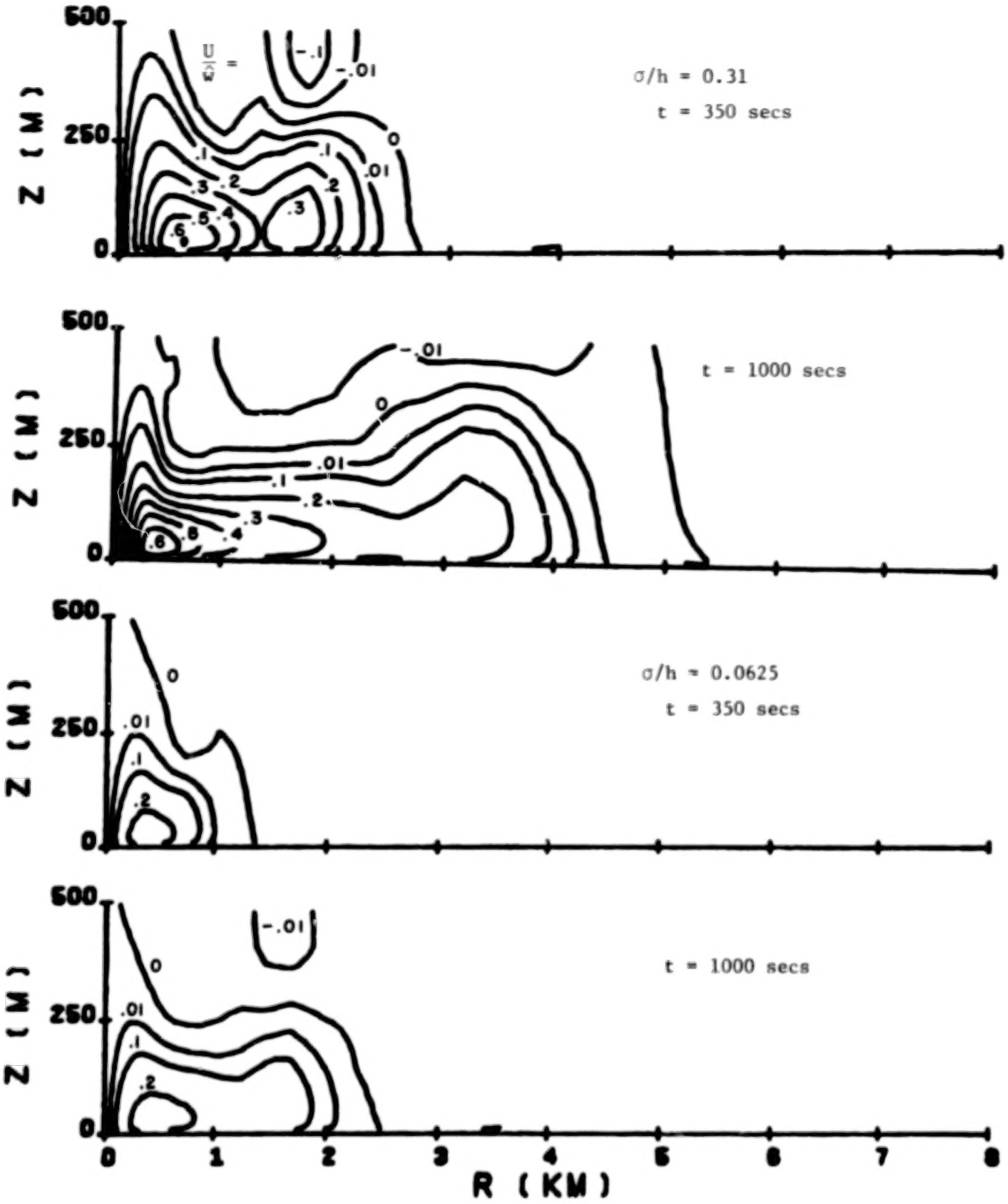

Figure 7. Contours of constant horizontal velocity as a function of r and z at t = 350 secs and 1000 secs ($t\hat{W}/h$ = 5 & 14.3) for σ/h = 0.31 and 0.0625.

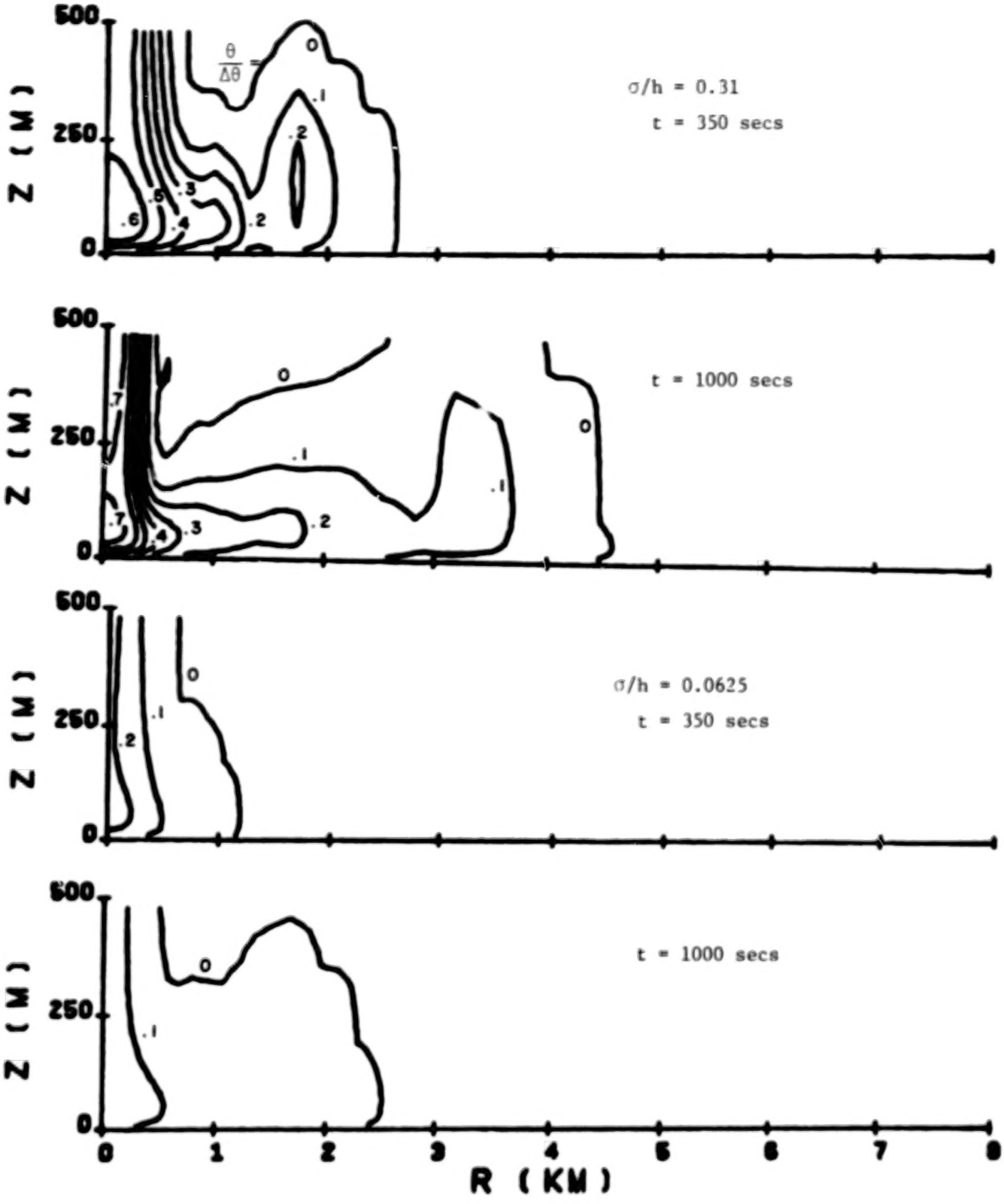

Figure 8. Contours of constant potential temperature as a function of r and z at t = 350 secs and 1000 secs ($t\Omega/h$ = 5 & 14.3) for σ/h = 0.31 and 0.0625.

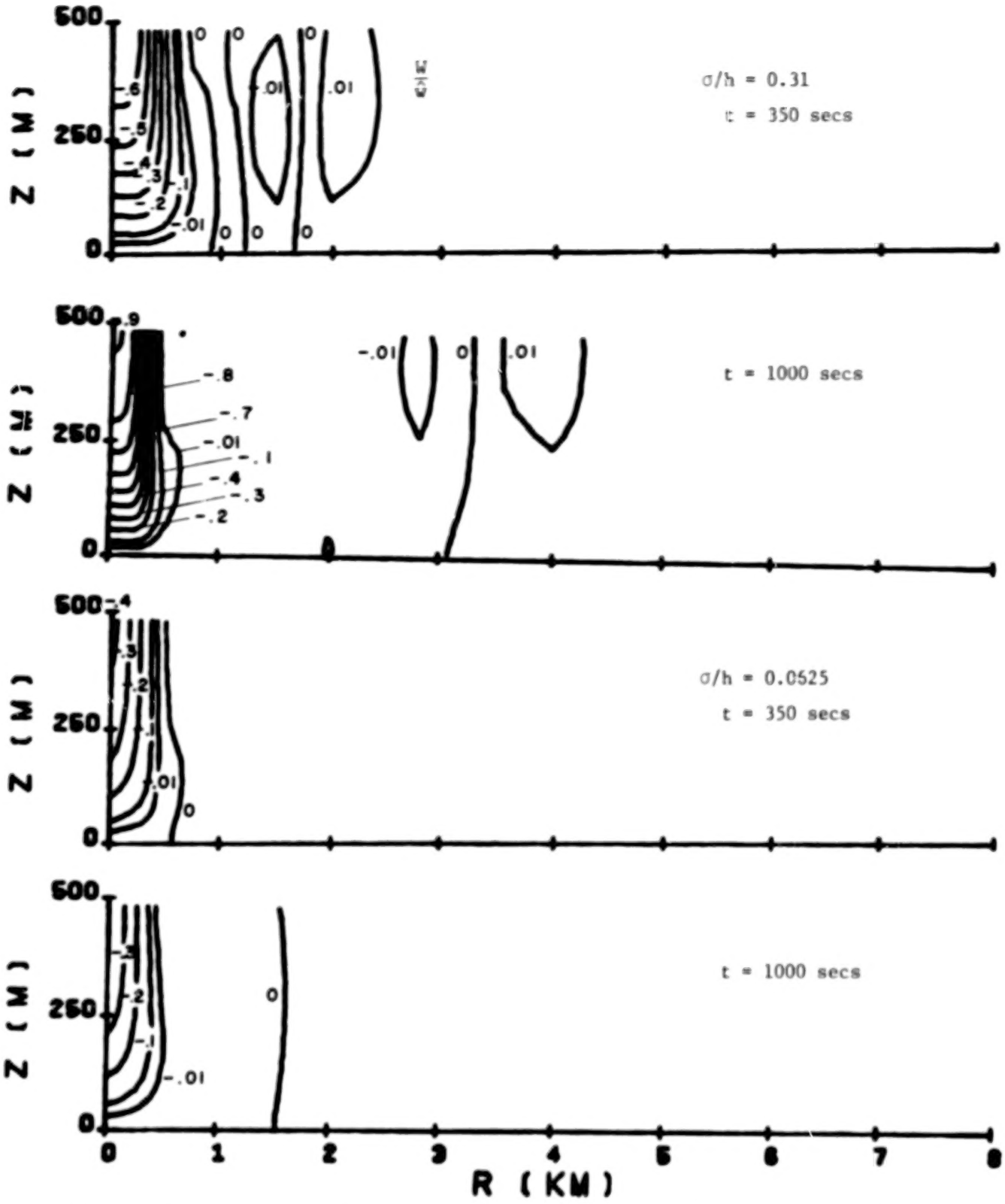

Figure 9. Contours of constant vertical velocity as a function of r and z at t = 350 secs and 1000 secs ($t\Omega/h$ = 5 & 14.3) for σ/h = 0.31 and 0.0625.

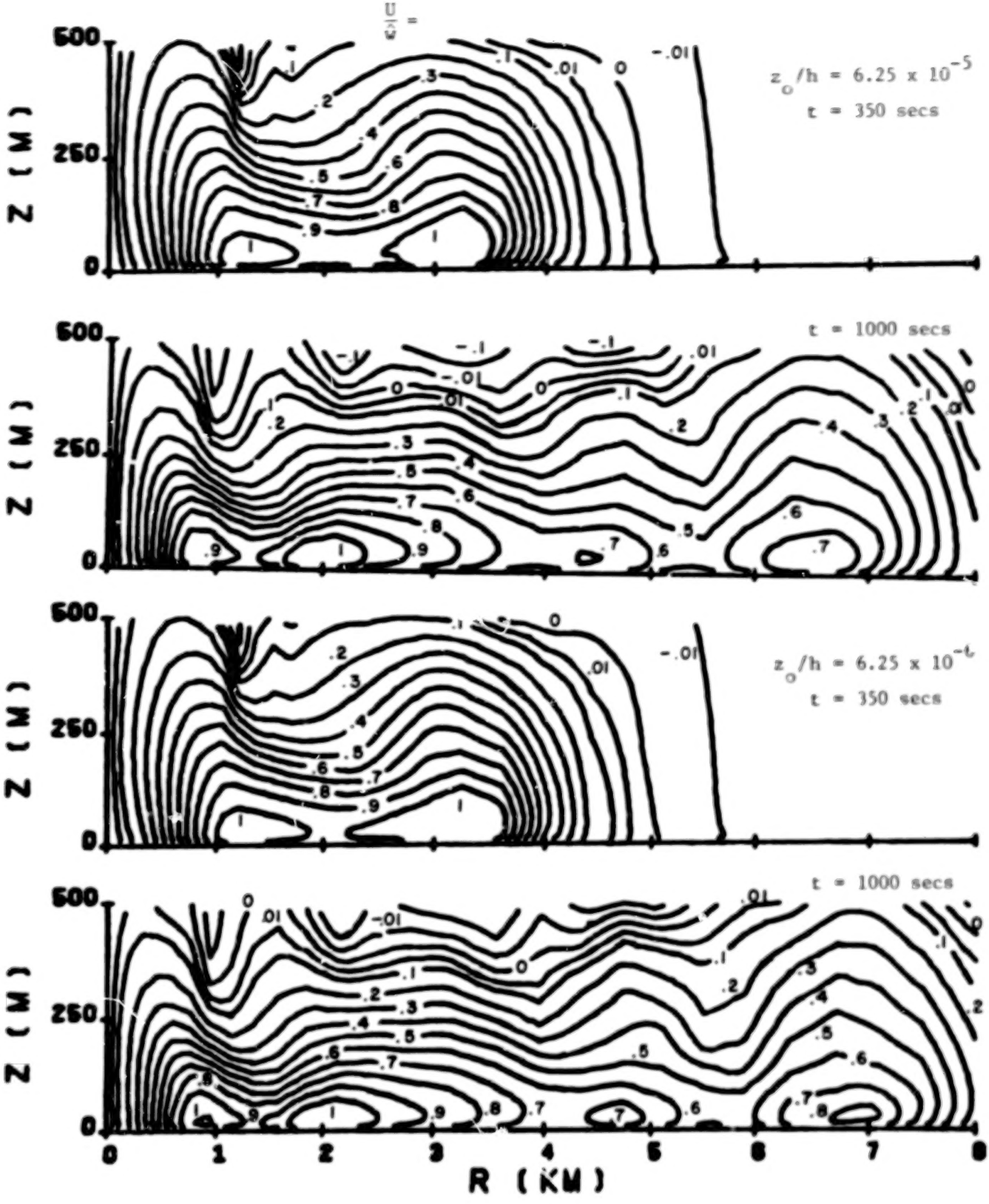

Figure 10. Contours of constant horizontal velocity as a function of r and z at t = 350 secs and 1000 secs for $z_o/h = 6.25 \times 10^{-5}$ and 6.25×10^{-6}.

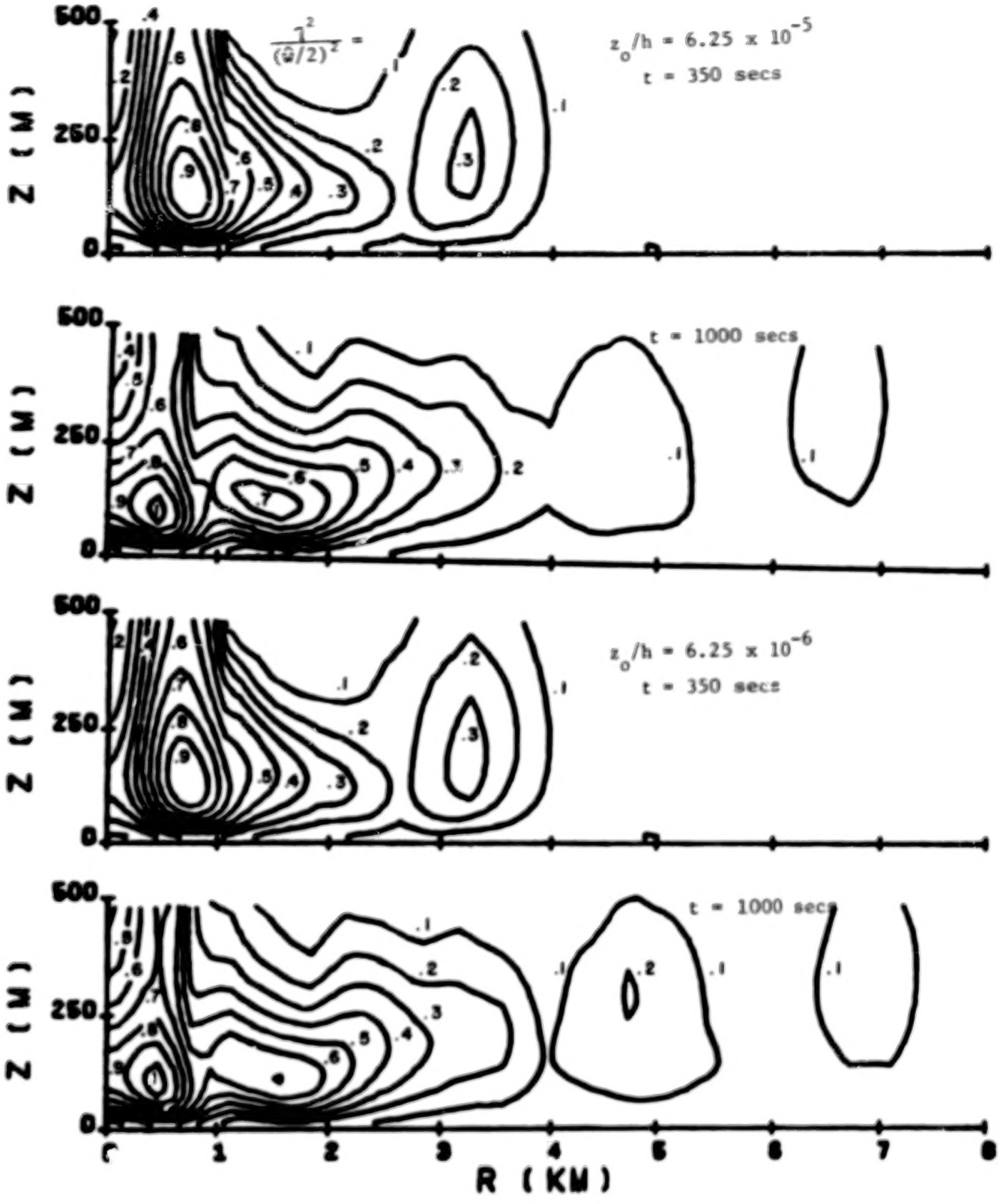

Figure 11. Contours of constant total velocity variance as a function of r and z at t = 350 secs and 1000 secs for $z_o/h = 6.25 \times 10^{-5}$ and 6.25×10^{-6}.

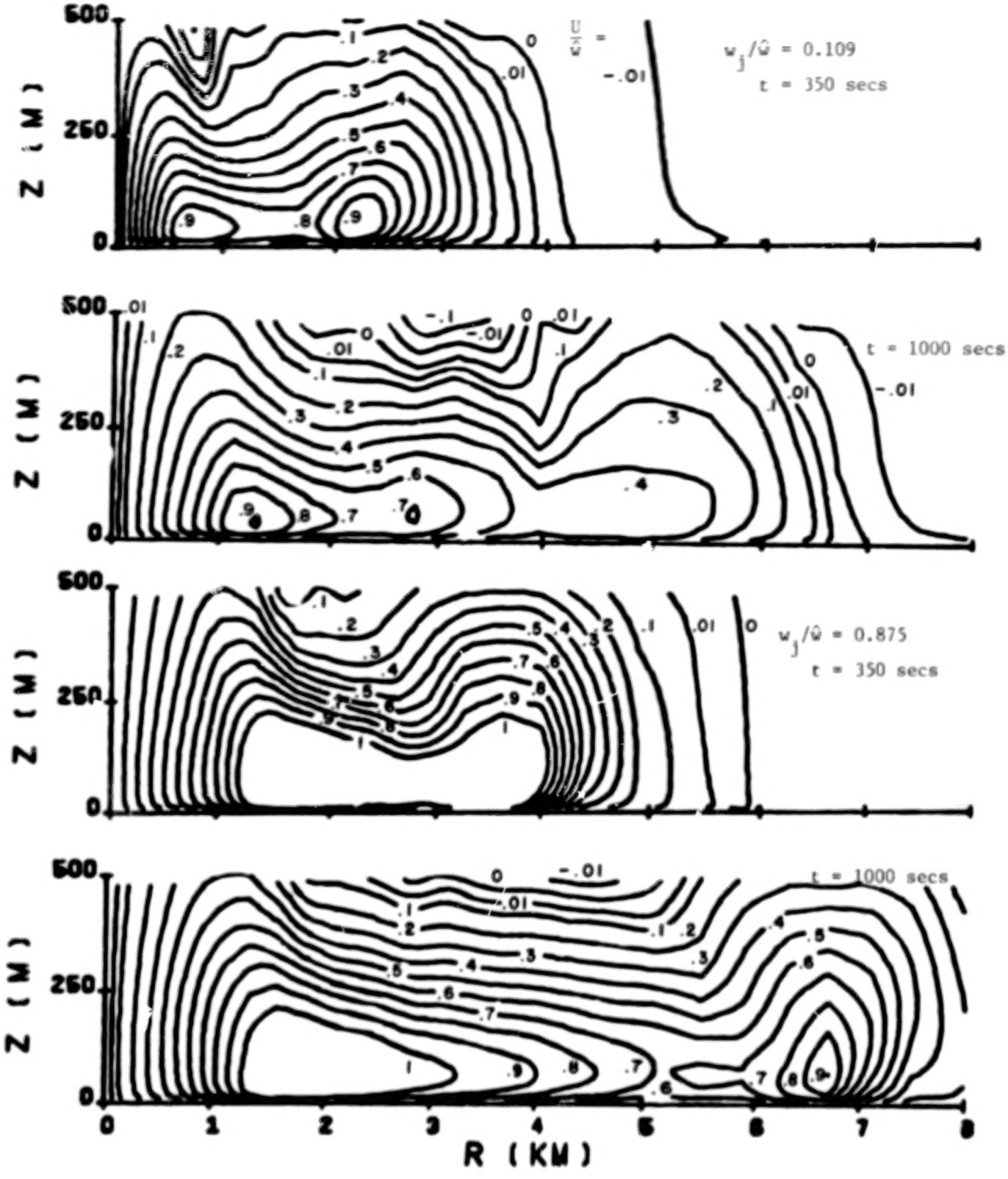

Figure 12. Contours of constant horizontal velocity as a function of r and z at t = 350 secs and 1000 secs for $w_j/\hat{w}$ = 0.109 and 0.875.

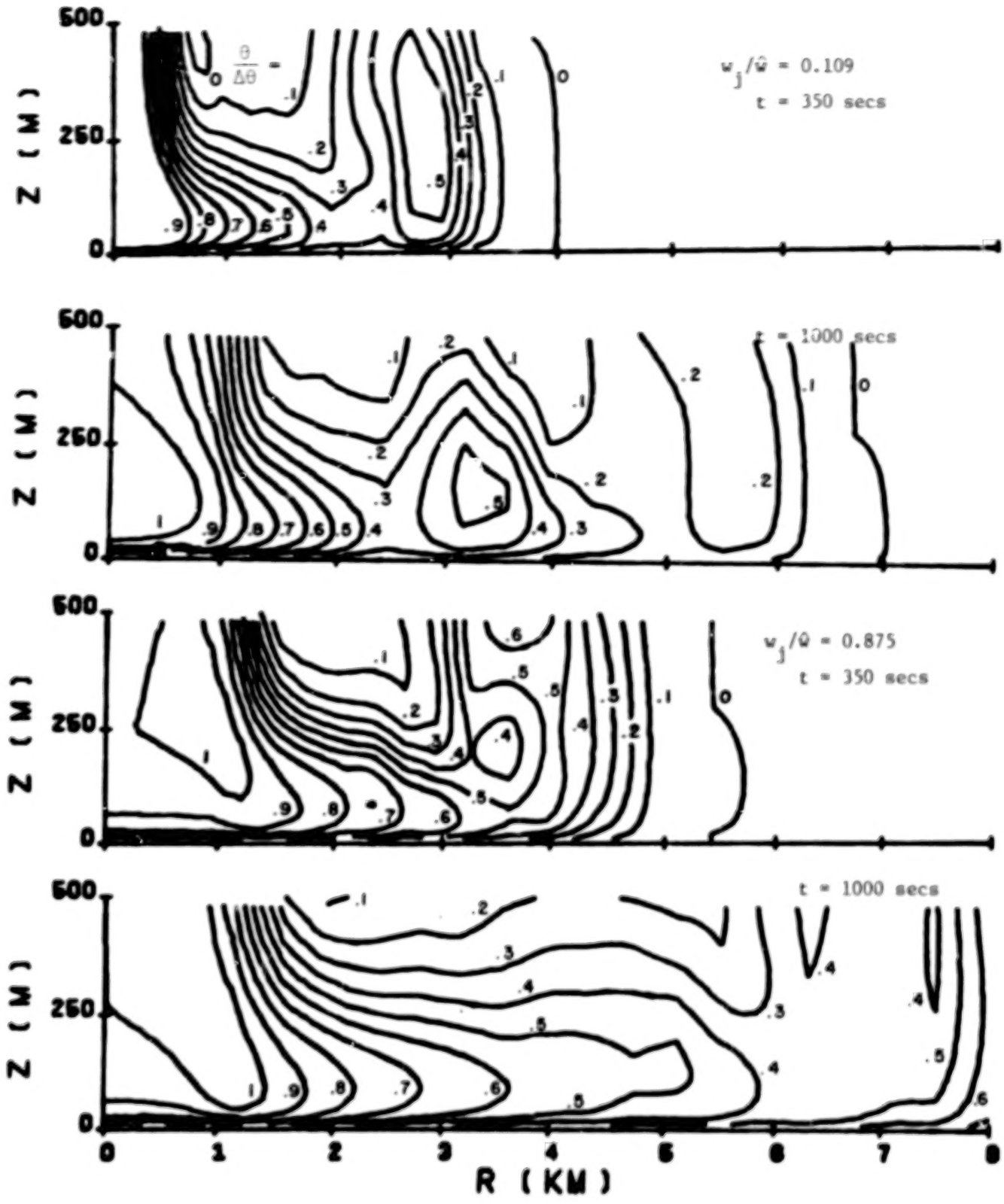

Figure 13. Contours of constant potential temperature as a function of r and z at t = 350 secs and 1000 secs for $w_j/\bar{w}$ = 0.109 and 0.875.

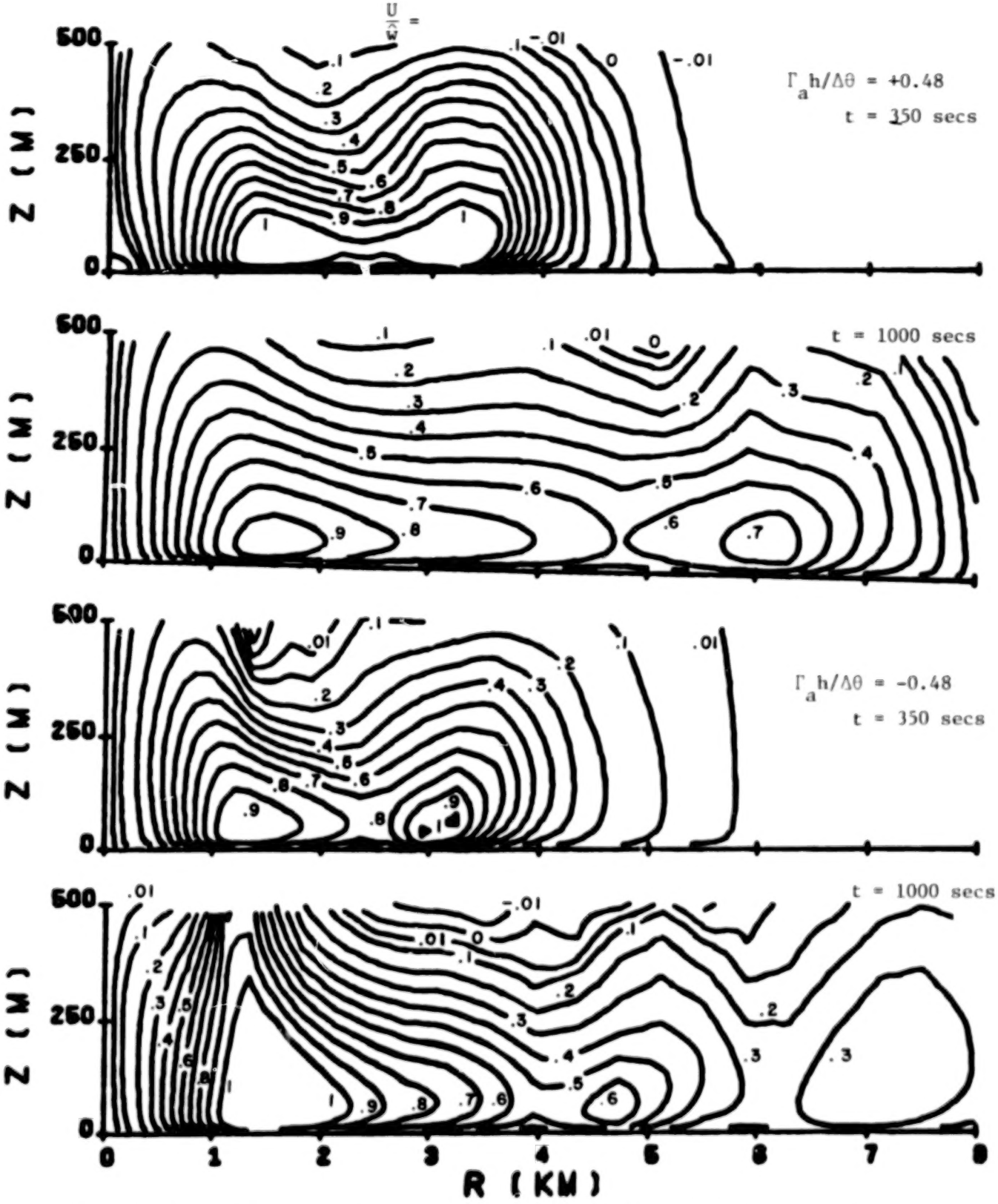

Figure 14. Contours of constant horizontal velocity as a function of r and z at t = 350 secs and 1000 secs for $\Gamma_a h/\Delta\theta$ = 0.48 and -0.48.

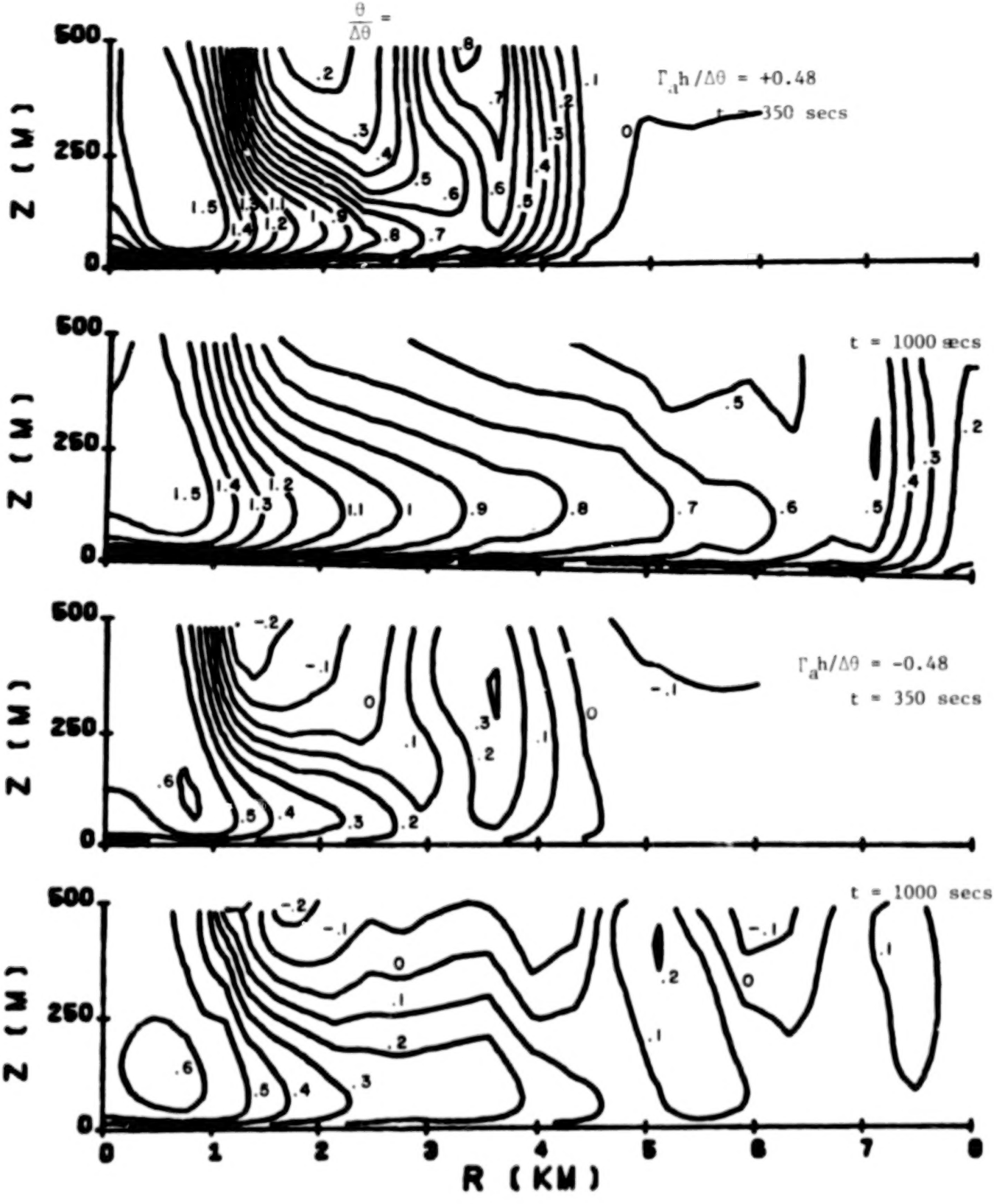

Figure 15. Contours of constant potential temperature as a function of r and z at t = 350 secs and 1000 secs for $\Gamma_a h/\Delta\theta$ = 0.48 and -0.48.

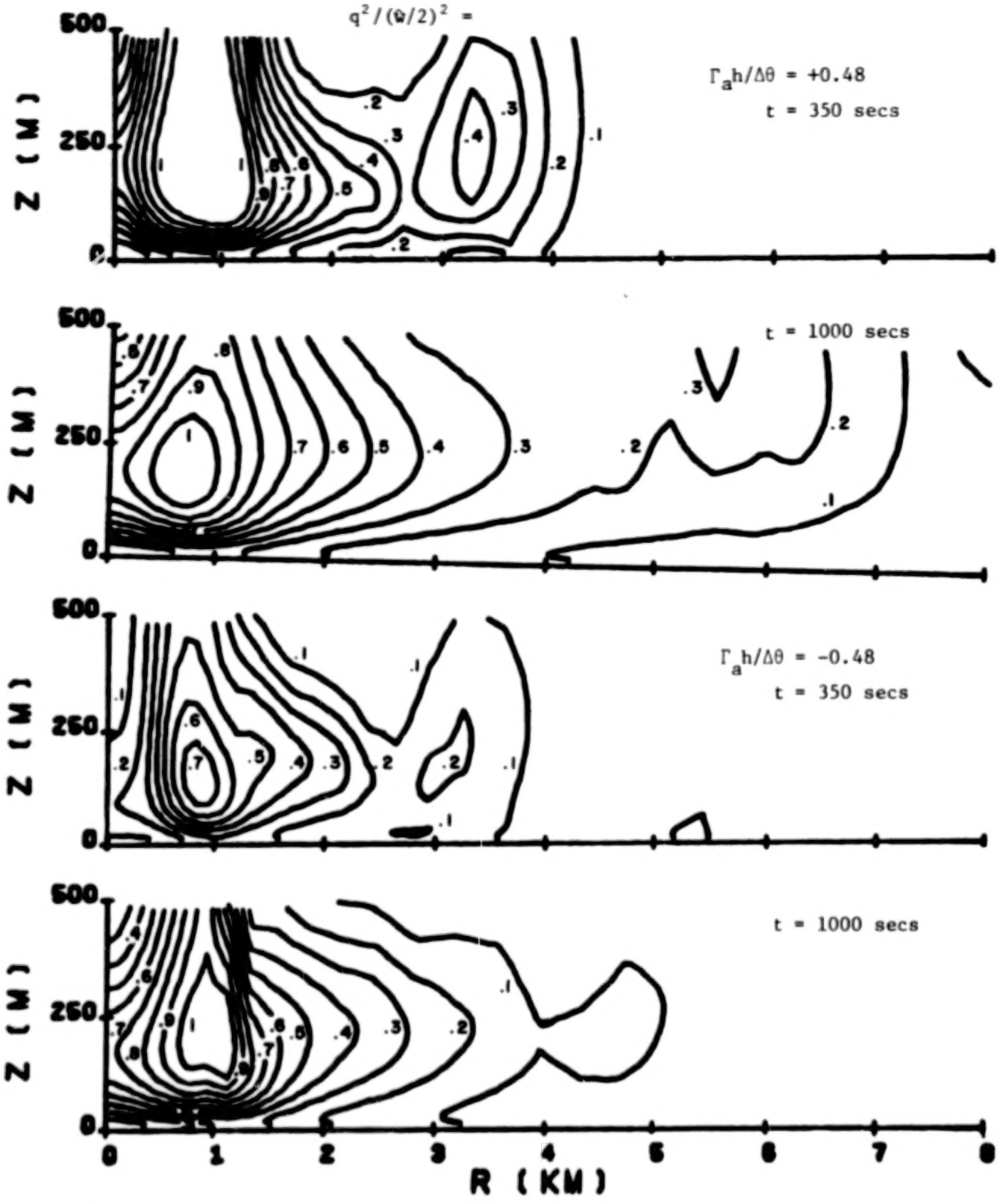

Figure 16. Contours of constant total velocity variance as a function of r and z at t = 350 secs and 1000 secs for $\Gamma_a h/\Delta\theta$ = 0.48 and -0.48.

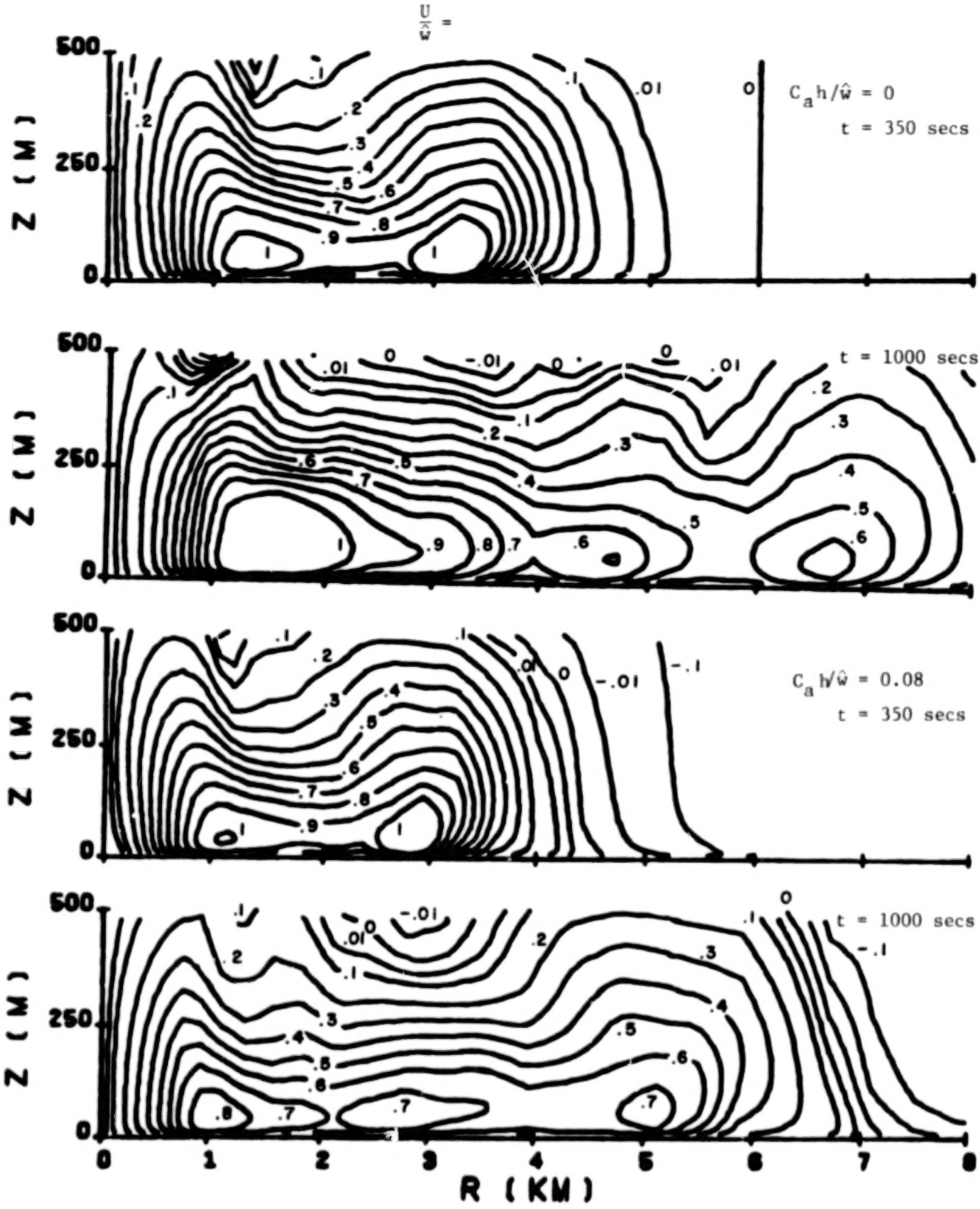

Figure 17. Contours of constant horizontal velocity as a function of r and z at t = 350 secs and 1000 secs for $C_a h/\hat{w}$ = 0 and 0.08.

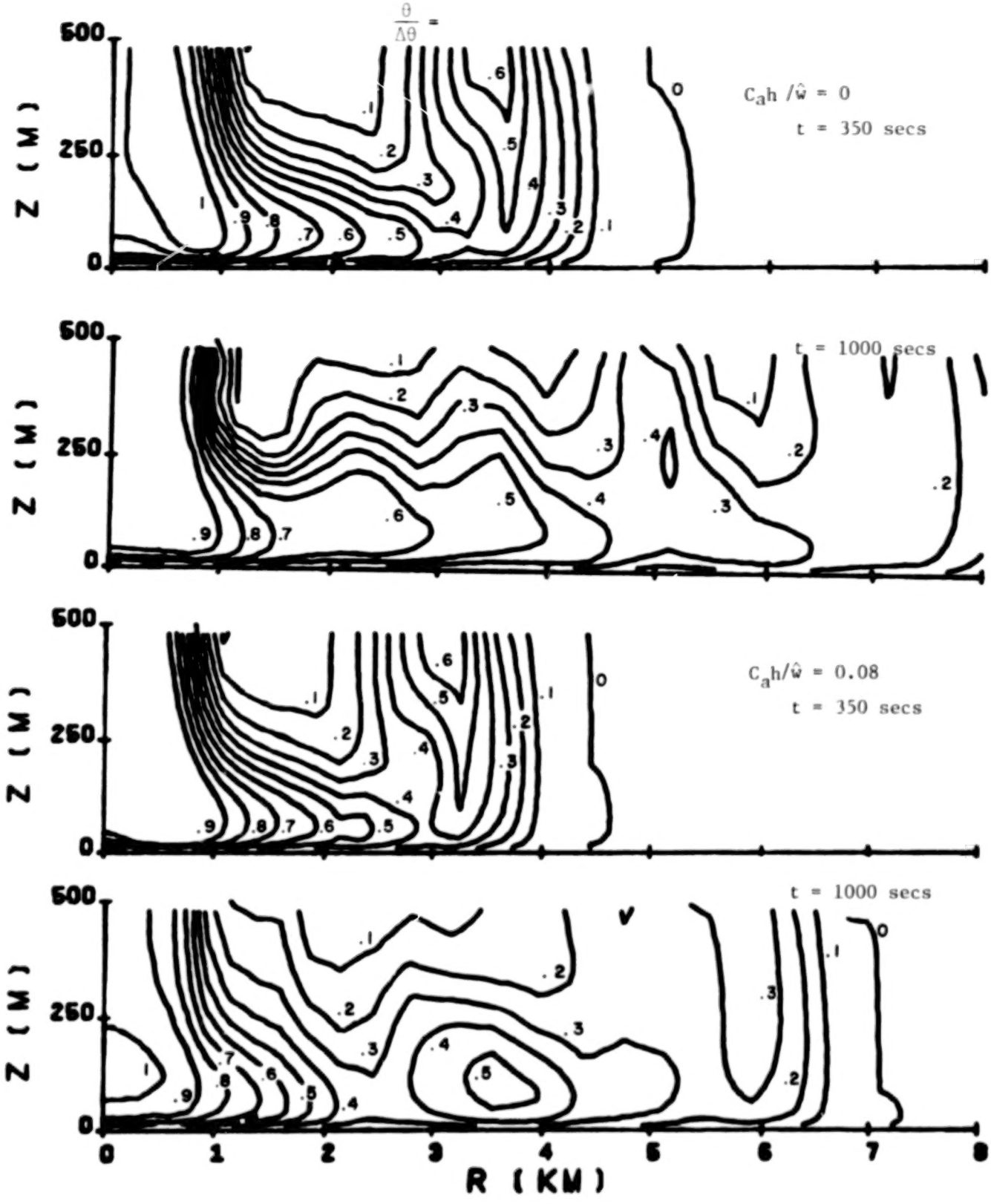

Figure 18. Contours of constant potential temperature as a function of r and z at t = 350 secs and 1000 secs for $C_a h/\hat{w}$ = 0 and 0.08.

It has even less influence at earlier times in the simulation. At large distances from the center of the downdraft, it does aid in slowing the advance of the gust front.

In nature, the downdraft is seldom if ever precisely axisymmetric. We can partially determine the influence of geometry by studying the changes induced by converting from an axisymmetric simulation to a planar, two-dimensional simulation. This is shown in Fig. 19. In this Cartesian case, the gust front moves more rapidly than its axisymmetric counterpart and maintains its strength out to greater horizontal distances. This difference appears to be brought about directly by continuity in the outflow layer. With the flow cross-sectional area increasing with increasing r in the axisymmetric case, either the outflow velocity or the depth of the outflow must decrease. This area change does not exist in the Cartesian case.

The results of simulating the limiting case of a neutral downdraft is shown in Fig. 20. In this case the characteristic normalizing velocity is taken as the velocity of the downdraft at the top of the domain. The flow is that of a turbulent stagnating jet with no influence of gravity. In addition to the scaling down of the velocities, the character of the flow is quite different with no distinct gust front.

In all of the previous simulations the potential temperature defect is prescribed by inflow conditions at the top of the domain and there are no energy sources or sinks within the flow. As a result of a separate contract for the Naval Air System Command, we have been able to incorporate water change of phase into our Cartesian case (Ref. 14). This permits us to simulate evaporative cooling which is nature's forcing function for the potential temperature defect. Figures 21 to 24 show the results of repeating the previous calculation for no $\Delta\theta$ in the downdraft at the top of the domain, but permitting it to have a liquid water content. The maximum virtual potential temperature defect is 5.6 and occurs 300 secs after the start of the run. The absolute temperature of the air actually rises as the air moves down into regions of higher pressure by compression. But in order to stay saturated at the higher absolute temperature, it evaporates some of the liquid water present and is cooler than it would be if it descended along a dry adiabatic curve. Evaporative cooling allows the velocity in this case to reach a value which is 2.5 times larger than that for the neutral downdraft.

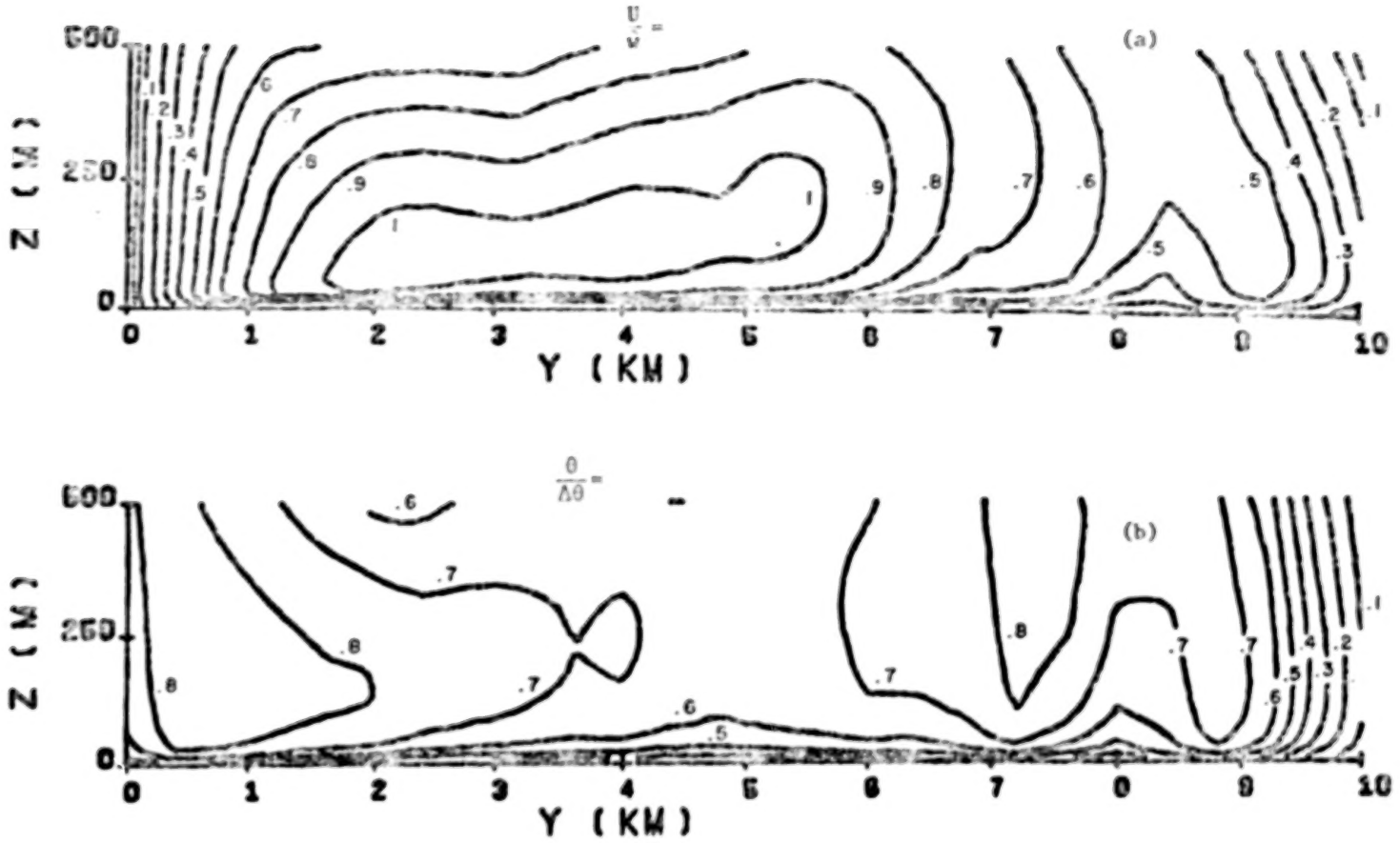

Figure 19. Flow variables as a function of y and z at t = 1000 secs for the simulated planar downdraft; (a) horizontal velocity, (b) potential temperature, (c) vertical velocity, and (d) total velocity variance.

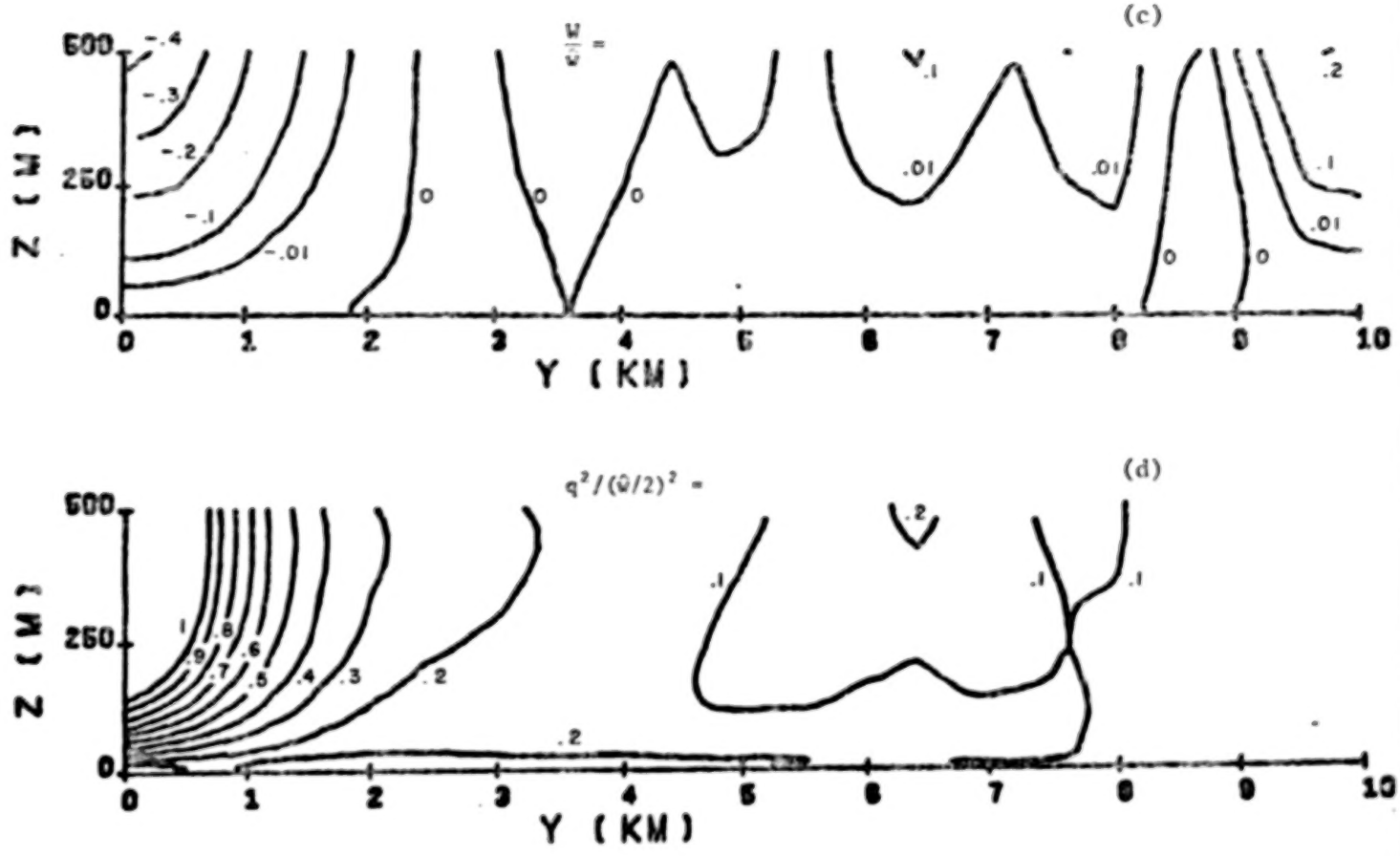

Figure 19 (continued).

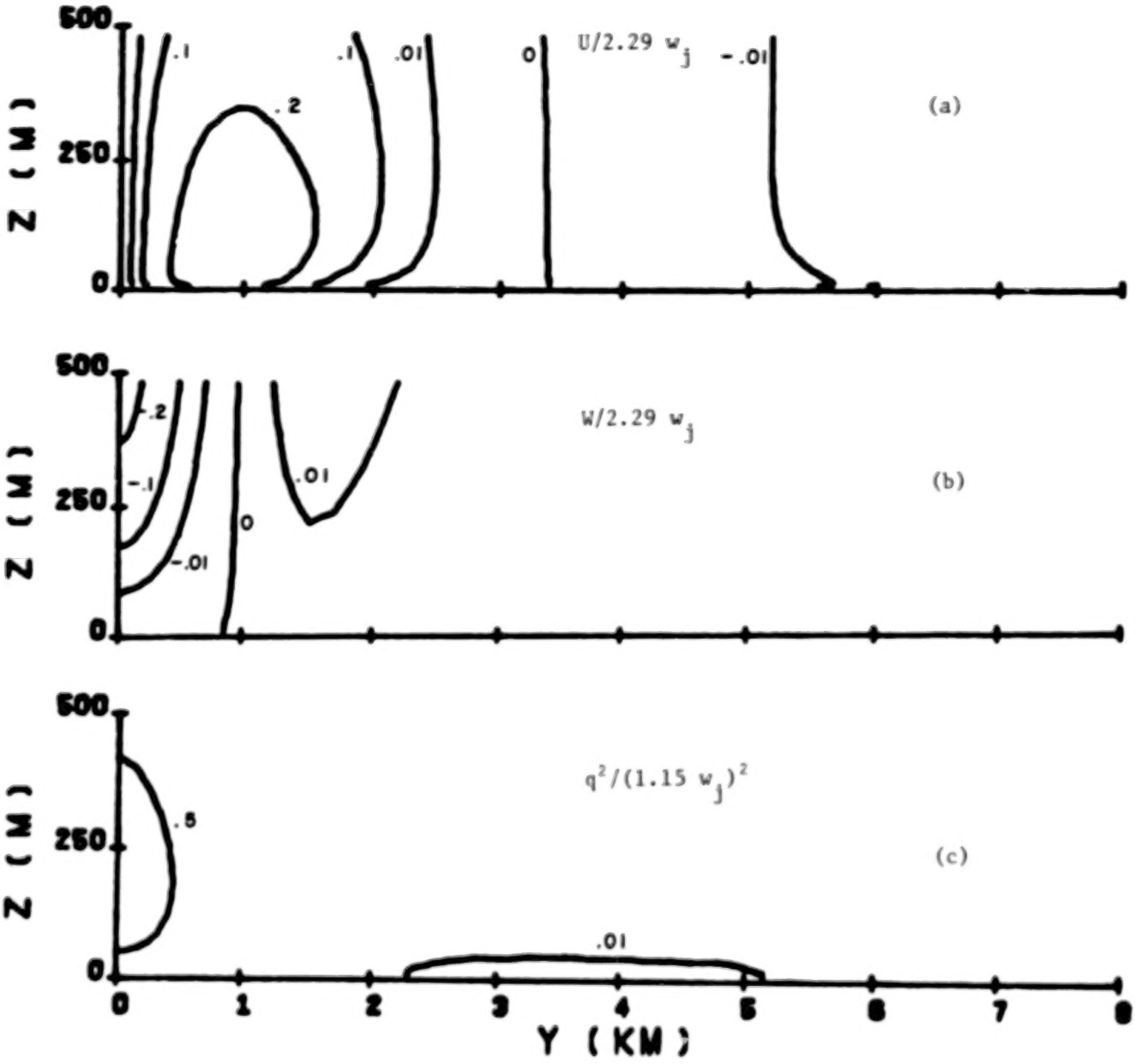

Figure 20. Contours of constant (a) horizontal velocity, (v) vertical velocity, (c) total velocity variance for $w_j/\hat{w} = \infty$ at t = 500 secs.

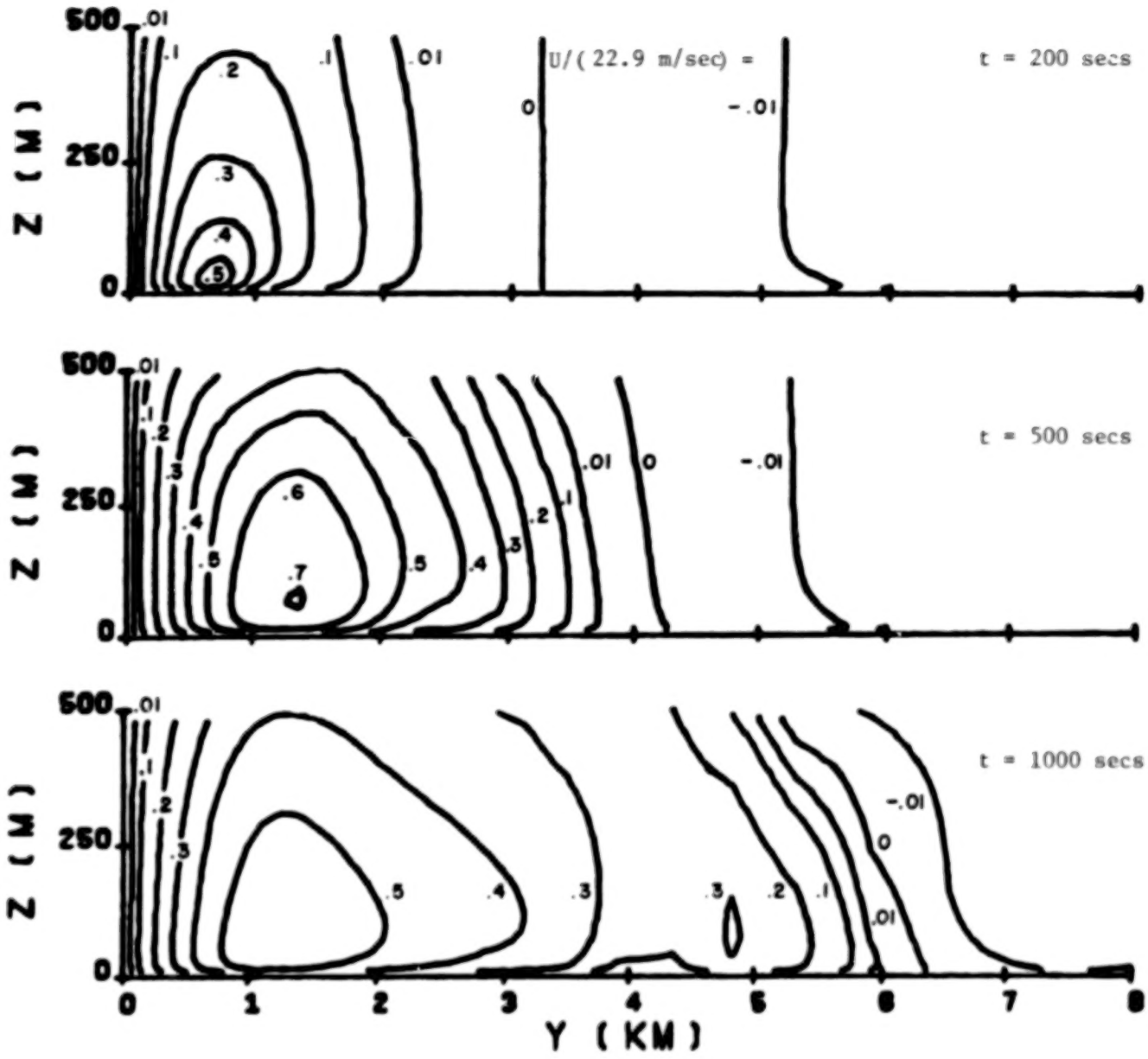

Figure 21. Contours of constant horizontal velocity for the downdraft of Fig. 20 with evaporation at t = 200, 500 and 1000 secs.

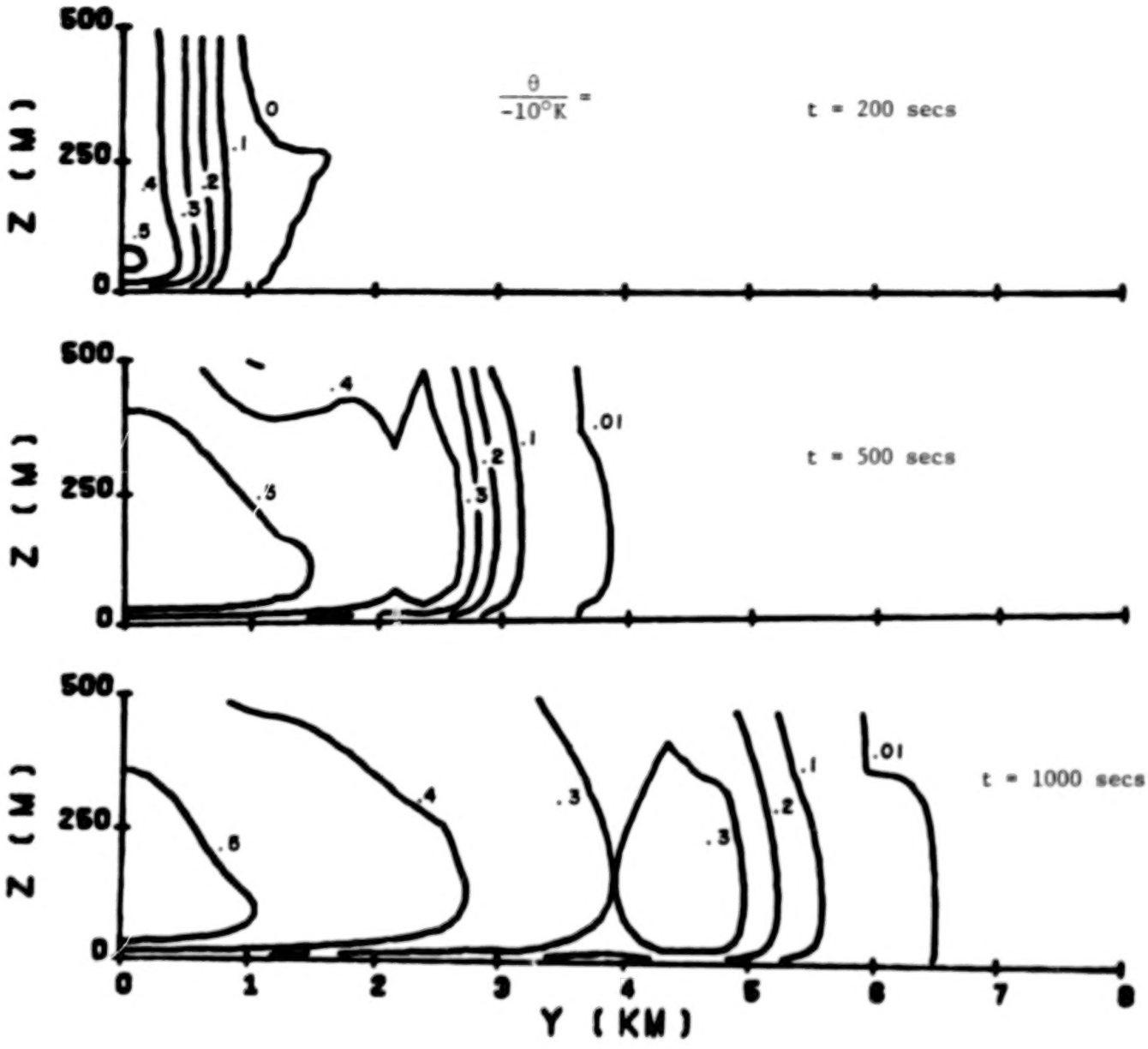

Figure 22. Contours of constant potential temperature for the downdraft of Fig. 20 with evaporation at t = 200, 500 and 1000 secs.

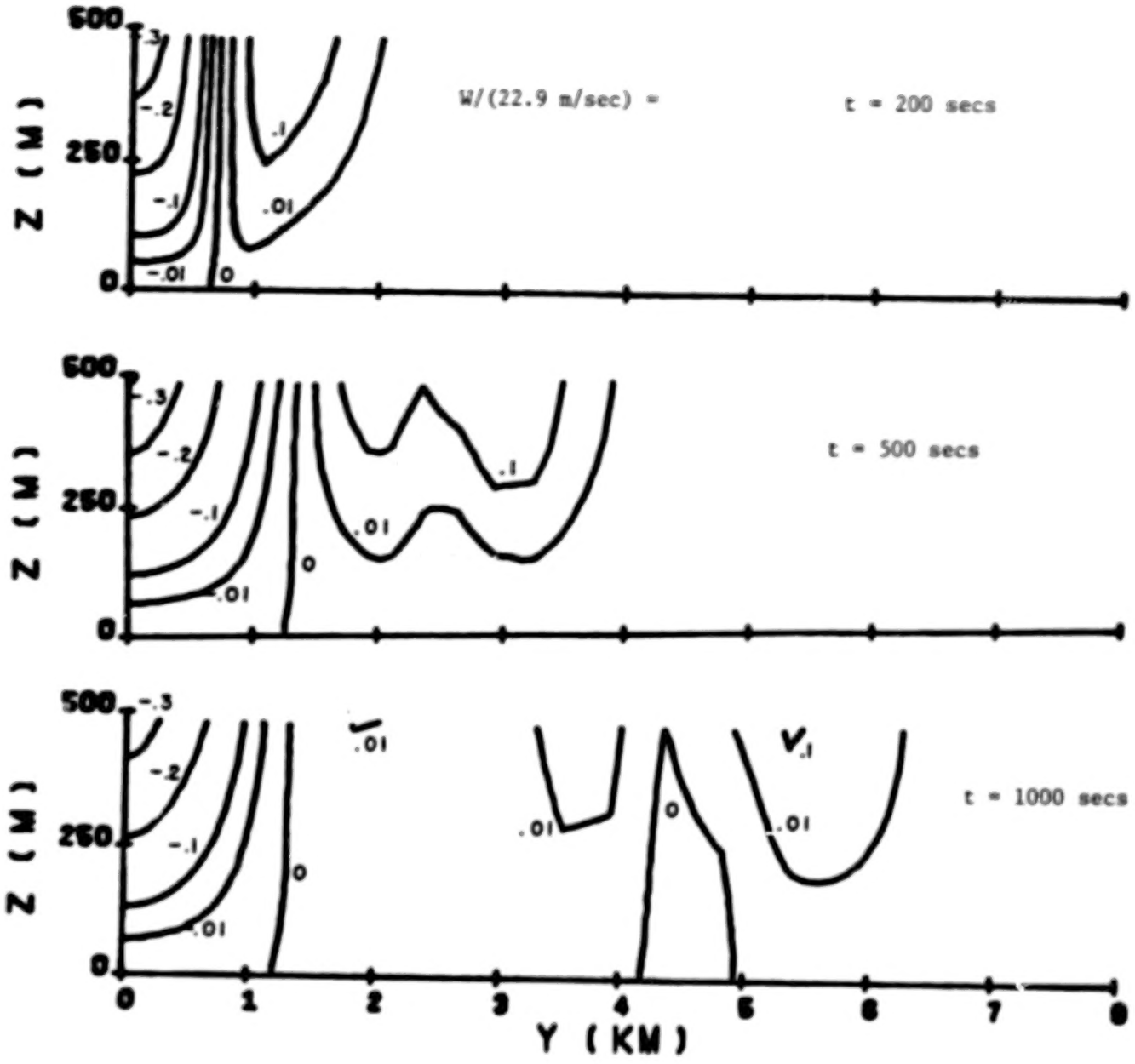

Figure 23. Contours of constant vertical velocity for the downdraft of Fig. 20 with evaporation at t = 200, 500 and 1000 secs.

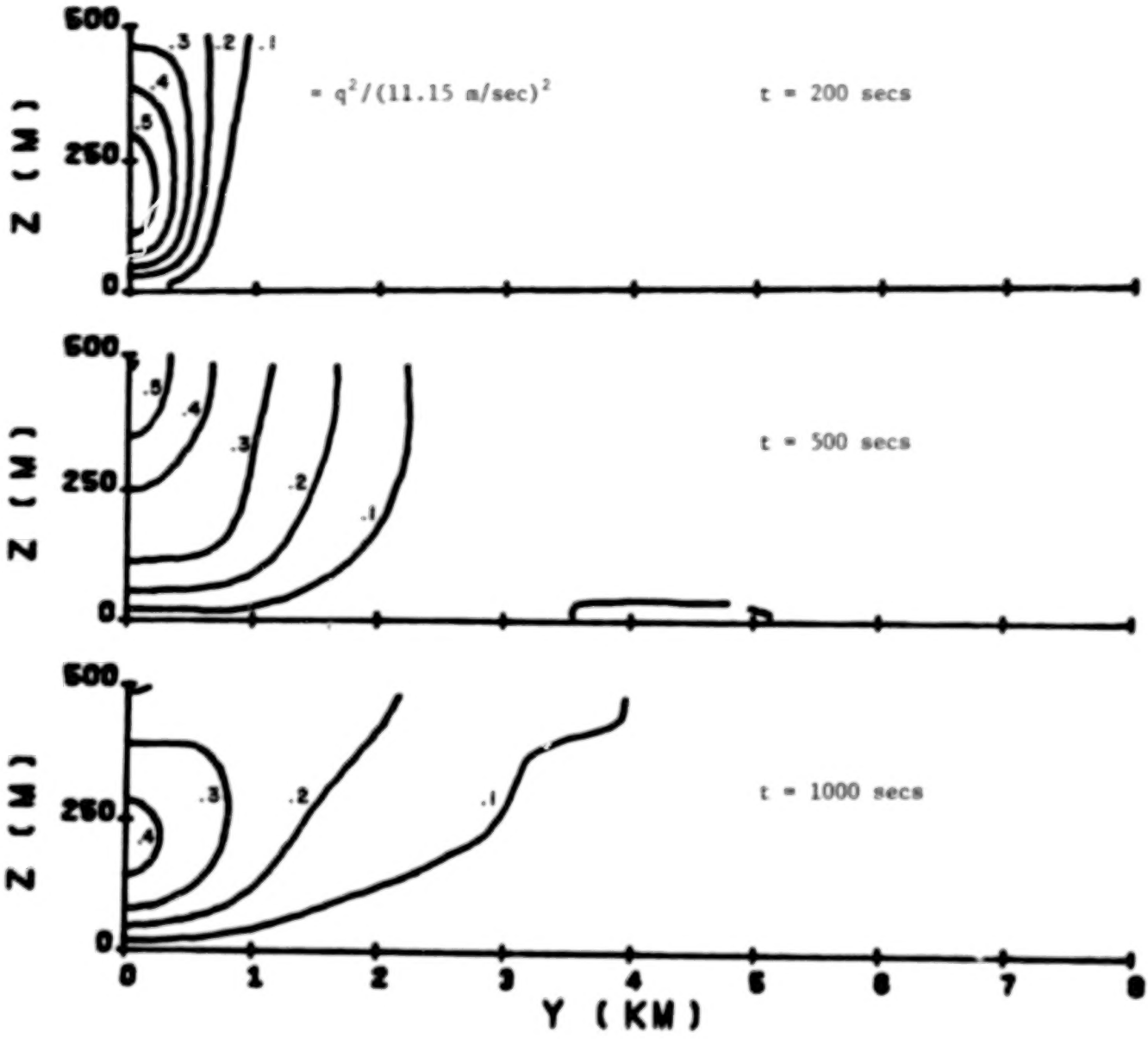

Figure 24. Contours of constant total velocity variance for the downdraft of Fig. 20 with evaporation at t = 200, 500 and 1000 secs.

Pressure Distributions

Since efforts are underway to develop gust front detectors based on pressure jump sensors (Refs. 15 and 16), we include model predictions of pressure perturbation distributions in Figs. 25 to 28. Figure 25 shows the time evolution of the Δp for our base case. To interpret the results for other values of $\Delta\theta$ and h, Δp should scale linearly with $-g\Delta\theta h$. Note that the modest pressure rise associated with the gust front is followed by a pressure dip before the steady climb to the max Δp on the centerline.

The pressure distribution for smaller σ/h is shown in Fig. 26. This decrease in downdraft σ decreases the pressure jump associated with the gust front. On the other hand, Fig. 27 shows that increasing the mass flow of cold air by increasing $w_j/\hat{w}$ increases the pressure jump associated with the gust. The surface roughness has a much more modest influence on Δp, as may be seen in Fig. 28.

Conditions Leading to Most Severe Wind Shear

The strongest wind shear conditions are likely to occur under the center of a moderately small diameter downdraft. For $\sigma/h \approx 0.3$, the downdraft is sufficiently large that the core can penetrate to the surface before the potential temperature defect is eroded by turbulent mixing, yet sufficiently narrow that the maximum radial outflow occurs at a small radius ($\approx 0.8h$). Under these conditions the horizontal wind shear will scale as $[(g|\Delta\theta|/T_o h)(1 + w_j^2/\hat{w}^2)]^{\frac{1}{2}}$. This appears to be the type of downdraft that occurred over the runway in Denver, Colorado on August 7, 1975. The simulated flight of a Continental Airlines 727 through such a downdraft was detailed in Ref. 2. The sharp loss in air-speed appeared more responsible for the aircraft accident than the negative mean vertical velocity.

Fujita (Ref. 10) defines a "downburst" as a downdraft with a vertical velocity greater than 3.6 m/sec at 91 m altitude. Due to the approximate linearity of the vertical velocity with respect to altitude near the surface, our model suggests that the vertical velocity at this particular reference height should also scale with $[(g|\Delta\theta|/T_o h)(1 + w_j^2/\hat{w}^2)]^{\frac{1}{2}}$. Our simulation case #2 suggests the proportionality constant is such that the downburst criterion will hold whenever

$$[(g|\Delta\theta|/T_o h)(1 + w_j^2/\hat{w}^2)]^{\frac{1}{2}} \geq 0.01 \qquad (3)$$

Although the wind shear conditions are not quite as strong near the gust front, they are perhaps more dangerous because such conditions can extend many kilometers away from the center of the

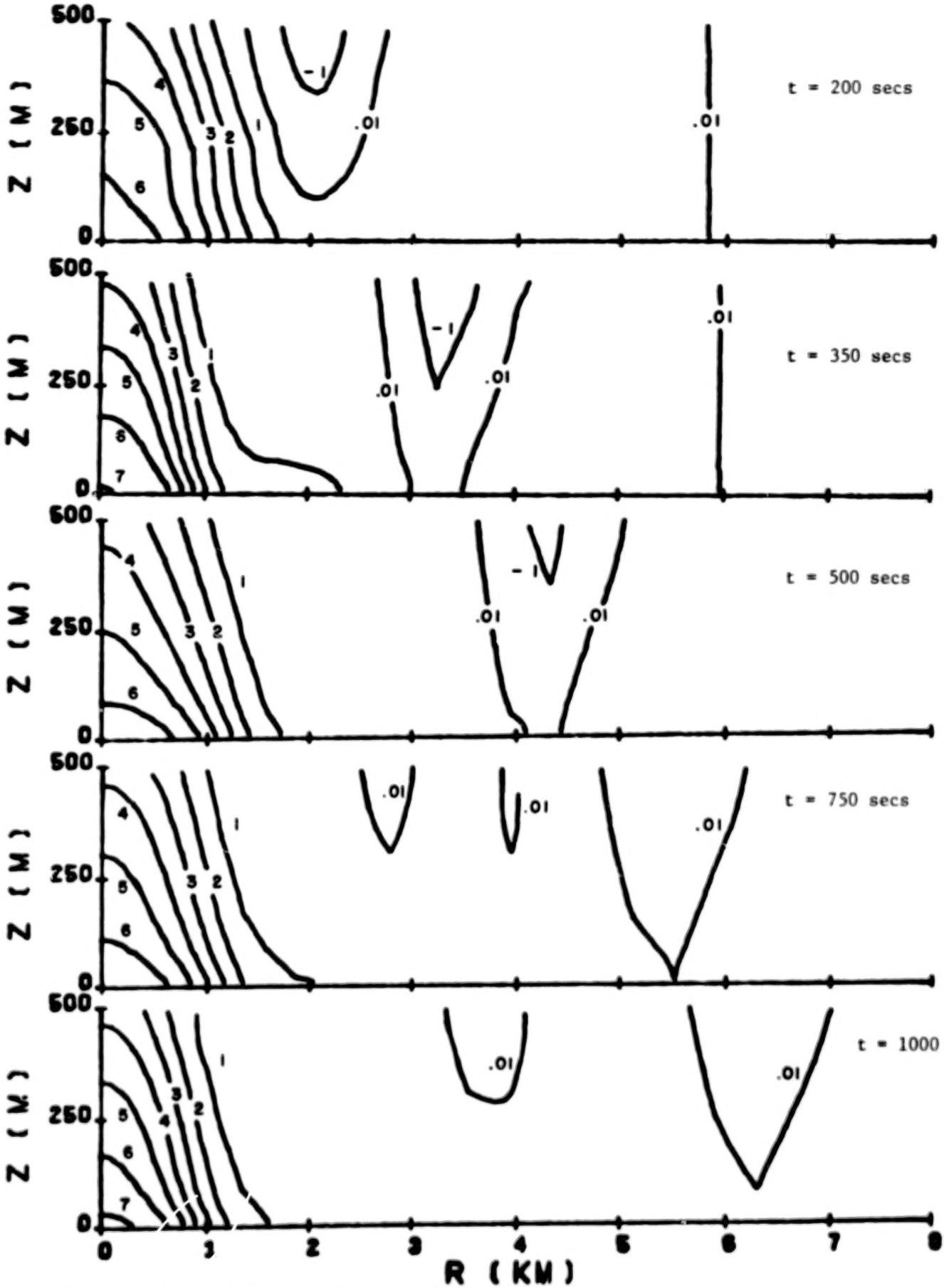

Figure 25. Contours of constant pressure perturbations for the base case at consecutive simulation times. Δp given in millibars for $\Delta\theta = -10^{\circ}K$, h = 1.6 km .

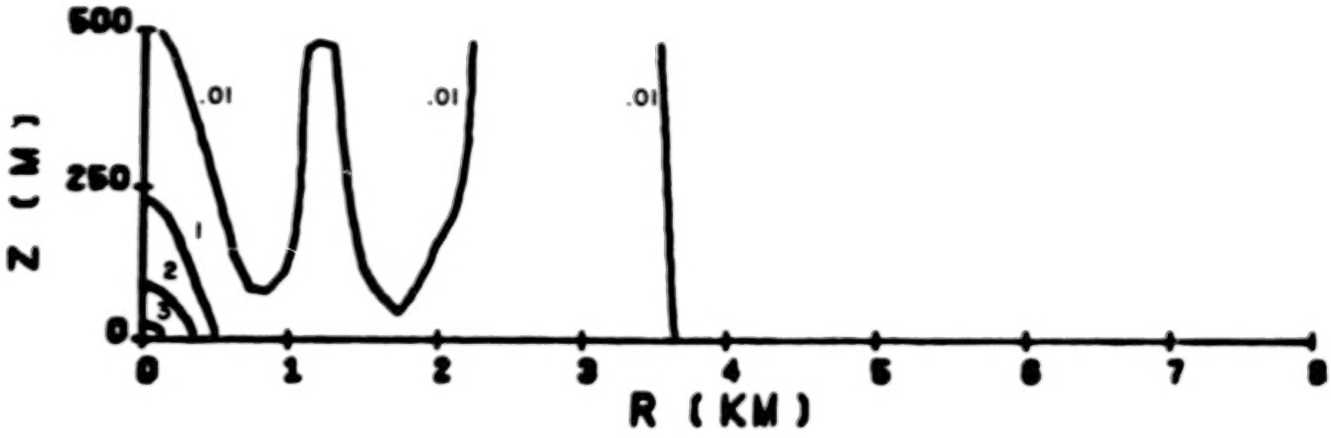

Figure 26. Contours of constant pressure perturbations for $\sigma/h = 0.31$ at $t = 350$. (Δp in millibars for $\Delta\theta = -10^{\circ}K$, $h = 1.6$ km)

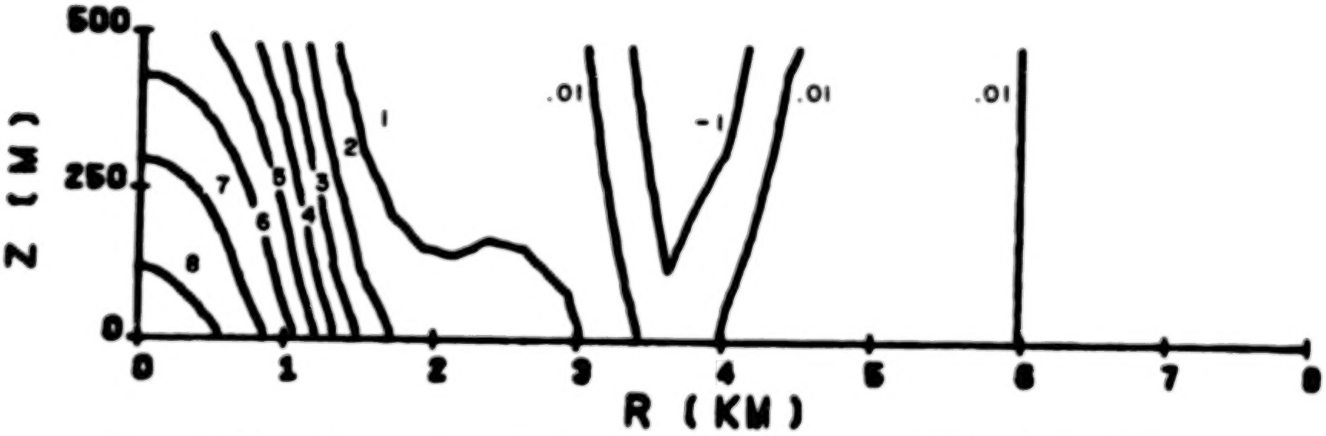

Figure 27. Contours of constant pressure perturbations for $w_j/\hat{w} = 0.875$ at $t = 350$. (Δp in millibars for $\Delta\theta = -10^{\circ}K$, $h = 1.6$ km)

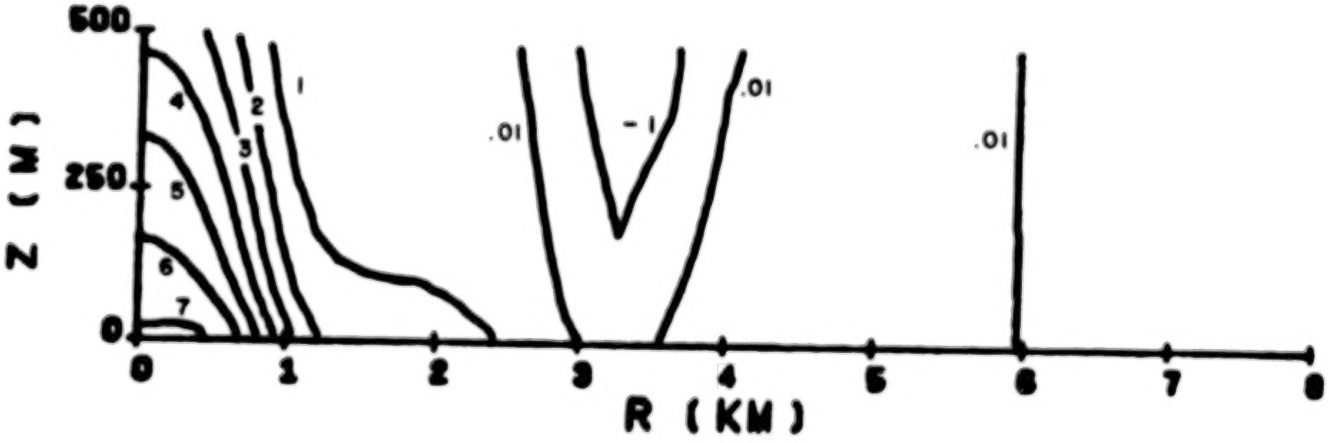

Figure 28. Contours of constant pressure perturbations for $z_o/h = 6.25 \times 10^{-6}$ at $t = 350$. (Δp in millibars for $\Delta\theta = -10^{\circ}K$, $h = 1.6$ km)

downdraft and are highly transient. Thus, the pilot is much more likely to be surprised by the gust front. From the preceding section it may be seen that decreasing the surface roughness, increasing the diameter of the downdraft, increasing the downdraft velocity at the top of the domain, increasing the potential temperature defect, and increasing the height at which the downdraft is released all add to the persistence of the gust front.

It is interesting to note that the conditions which lead to strong winds in the gust front several km from the center of the downdraft are not the same as those which lead to strong wind shear at the center. In particular, increasing h will decrease wind shear at the center while it increases vertical wind shear in the gust front at a large fixed radius.

III. WARM FRONT

The warm front is quite different from the thunderstorm gust front. It typically involves significant horizontal temperature gradients over distances of a few hundred kilometers. In our previous reports (Refs. 1 and 2), the influences of this baroclinicity was simulated by introducing a vertical gradient of the geostrophic wind into our one-dimensional planetary boundary layer model. This appears to give a quite valid representation of the boundary layer flow. The difficulty lies in determining appropriate geostrophic wind profiles. In the present section we use our two-dimensional model so that the pressure gradients may be internally determined by the dynamics of the front.

Well above the surface boundary layer the slope of a warm front is expected to be determined by the stable balance between hydrostatic and Coriolis forces as given by Margules' relationship (Ref. 16)

$$\text{Frontal Slope} = \frac{\Delta u_g f T_o}{g \Delta \theta} \tag{4}$$

Our simulation will impose this slope condition at the top of the domain. At the ground, the surface roughness and the ground temperature are specified. The vertical profiles of wind and turbulence far ahead and far behind the front, where there are no baroclinic effects, are set using the one-dimensional boundary layer model.

The largest source of uncertainty introduced into the model is the specification of the stream function across the top of the domain (2 km in the present computations). The slope condition of Eq. (4) was applied to the other model variables but we were unable to find a simple way of applying this constraint to the stream function. We guessed at the horizontal transition between the stream function value at 2 km height well ahead of the front and that well behind the front. We believe the results below 500 m altitude which are of primary interest to us, should be a valid simulation of that likely to occur in a front.

Scaling Relationships

The purpose of this section is to determine the dimensionless parameters that significantly affect the structure of a front, and to provide what information is available about what affect they have.

The only dimensional parameters entering the simulation as outlined in the previous section are Δu_g, $\Delta\theta$, g, T_o, f, u_g, v_g, z_o and $\theta_{surface}$, where U is taken parallel to

the front and V normal to the front. We could also formally include the viscosity and thermal conductivity of air. However, for the large Reynolds numbers appropriate for this atmospheric flow, the turbulent transport of momentum and heat will be determined by the flow with essentially no dependence on these two molecular transport coefficients. By taking the surface temperature to be in equilibrium with the air ahead of the front, we also eliminate $\theta_{surface}$ from the list. The remaining eight parameters can be grouped to form four independent dimensionless variables. These may be taken as

$$M = \frac{f\Delta u_g T_o}{g\Delta\theta} \quad , \qquad \text{Margules' parameters}$$

$$Ro = \frac{u_g}{fz_o} \quad , \qquad \text{a Rossby number}$$

and two velocity ratios $\Delta u_g/u_g$ and v_g/u_g .

In cases of principal interest for determining aviation hazards, we expect u_g on one side of the front to be much larger than that on the other side and also much larger than any normal velocities. Thus, in these interesting cases, the last two velocity ratios should remain roughly fixed at 1 and 0, respectively. This leaves the low-level warm front structure determined by M and Ro. Changing Ro affects the structure of the surface layer. However, in the neutral case, it was shown in Ref. 1 that appreciable changes (i.e., factors of 10-100) are required to exert a significant influence on this structure. In the next section, we show simulations of two fronts which are identical except that z_o is changed from 0.001 to 0.1 . This variation spans the range of major interest. It is seen that the structure of the front is only moderately influenced by this change. Thus, the effect of this parameter seems to be weak.

If the dependence of the solution on the two velocity ratios, $\Delta u_g/u_g$ and v_g/u_g , and on the Rossby number are neglected, then the variations with respect to M can be adsorbed by appropriate scaling of z and y . When z is normalized by $\Delta u_g/f$, y by $g\Delta\theta/T_o f$, θ by $\Delta\theta$, and all velocities by Δu_g then the slope of the front above the boundary layer will always be one in this normalized domain. The parameter M can then only enter the problem weakly through the other three parameters.

Simulation Results

Due to the large disparity between two characteristic times in this front calculation, it has proved to be a much more difficult numerical calculation than that of the gust front. The numerical time increments must remain small with comparison to the Brunt-Väisälä period of the most stable flow in the front. This limits the step-size to a few seconds. However, the simulation must be run for a few hours to permit Coriolis forces to be properly balanced. Consequently, approximately 1000 computational steps are required. Because of this, we have made a modification to the turbulence modeling to keep round-off errors from becoming a problem after this large number of steps.

Figures 29 to 32 show the results of a simulation with $M=0.006$ and $Ro = 10^8$. The flow was initialized by imposing a transition of all the primary variables from that for one-dimensional, barotropic flow far ahead of the front and far behind it. The transition is given a thickness of 100 km about a line with slope M. The figures show the structure of the front after approximately four hours of simulated time. During the run, all variables are held fixed on both sides which are 640 km apart. We show only the central part of the flow below 1 km altitude.

Figure 29 shows the mean wind parallel to the front. This is the component with the strongest wind shear. An aircraft descending through the air ahead of the front will have the wind first increasing and then decreasing. The horizontal variations occur slow enough that an aircraft descending on a 3° glide slope will be principally affected by the vertical wind shear.

The other principle flow variables which accompany Fig. 29 are shown in Figs. 30-32. The strong damping effect of the stable temperature gradient on the turbulence is readily apparent in Fig. 32. The horizontal gradients of all the variables are slightly stronger at the surface than they are at 1 km. Apparently the convergent flow induced by the surface layer has a stronger influence than the higher turbulence at the surface.

The effect of increasing surface roughness is shown in Figs. 33-36. The turbulence level near the surface on the cold side of the front is significantly higher. The other variables are changed remarkably little.

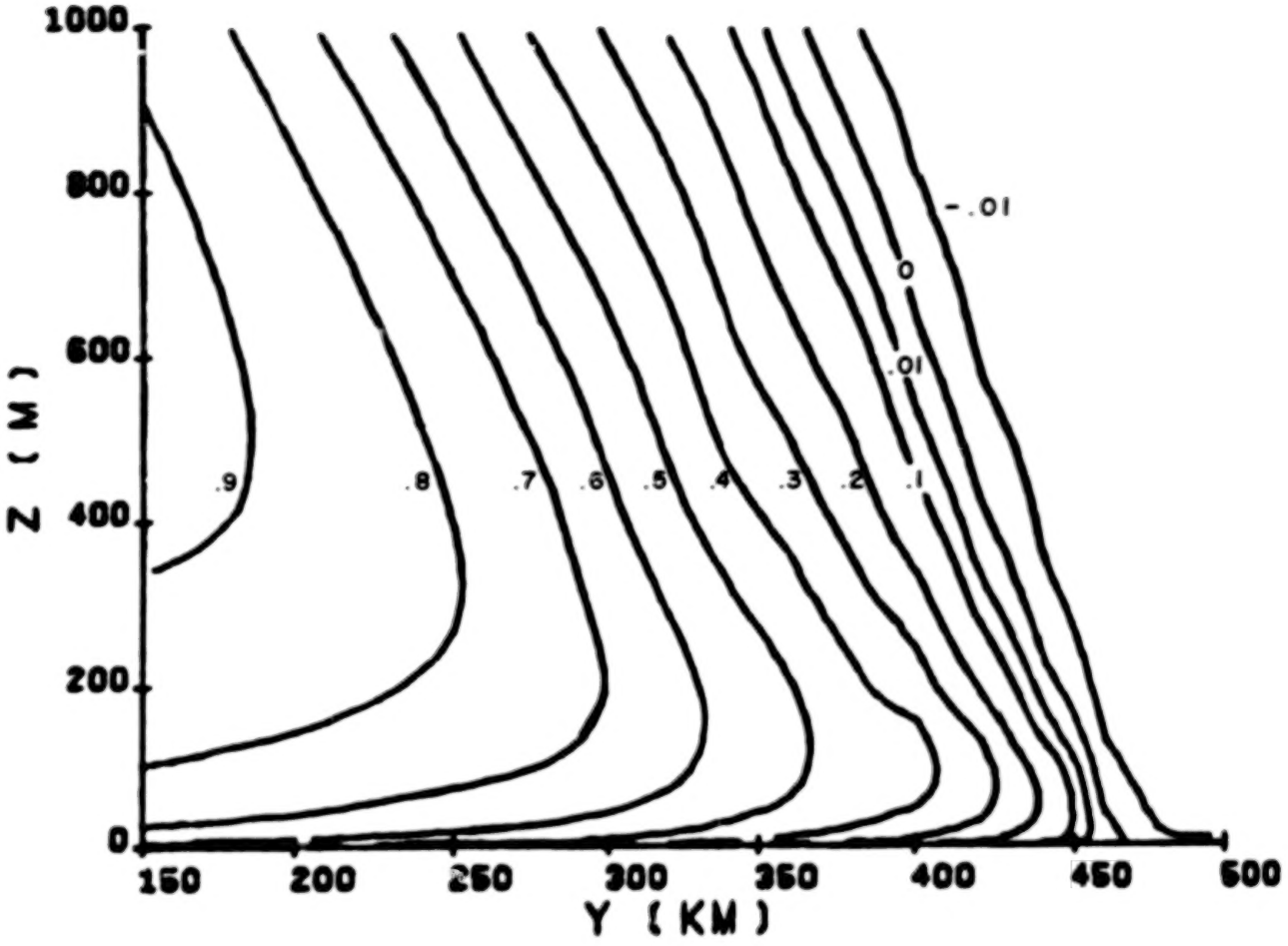

Figure 29. Distribution of mean wind parallel to a warm front near the surface for $Ro = 10^8$. Contours normalized by the total Δu_g across the front.

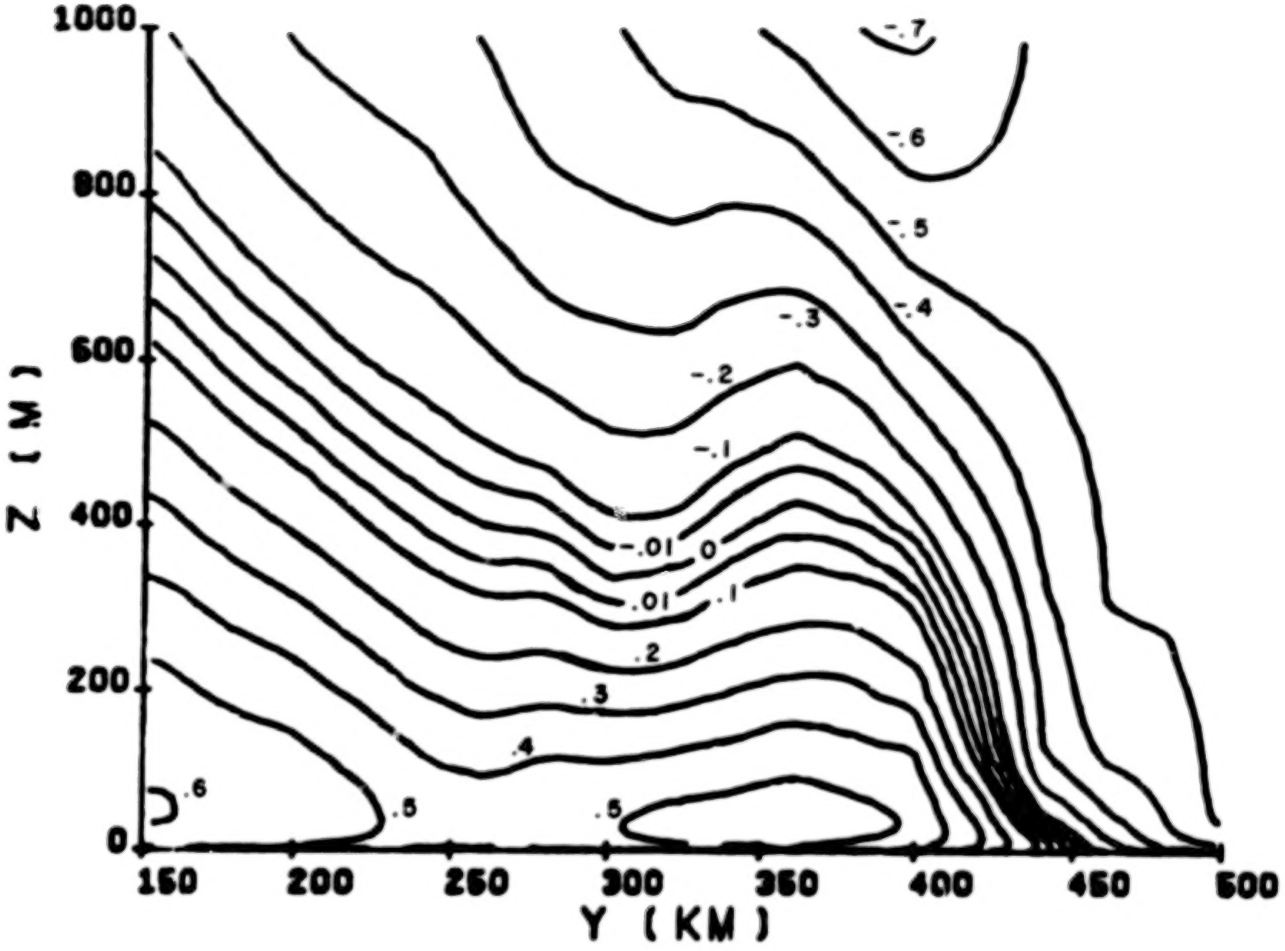

Figure 30. Distribution of mean wind normal to a warm front near the surface for $Ro = 10^8$. Contours normalized by $V_{max} = 0.18\Delta u_g$.

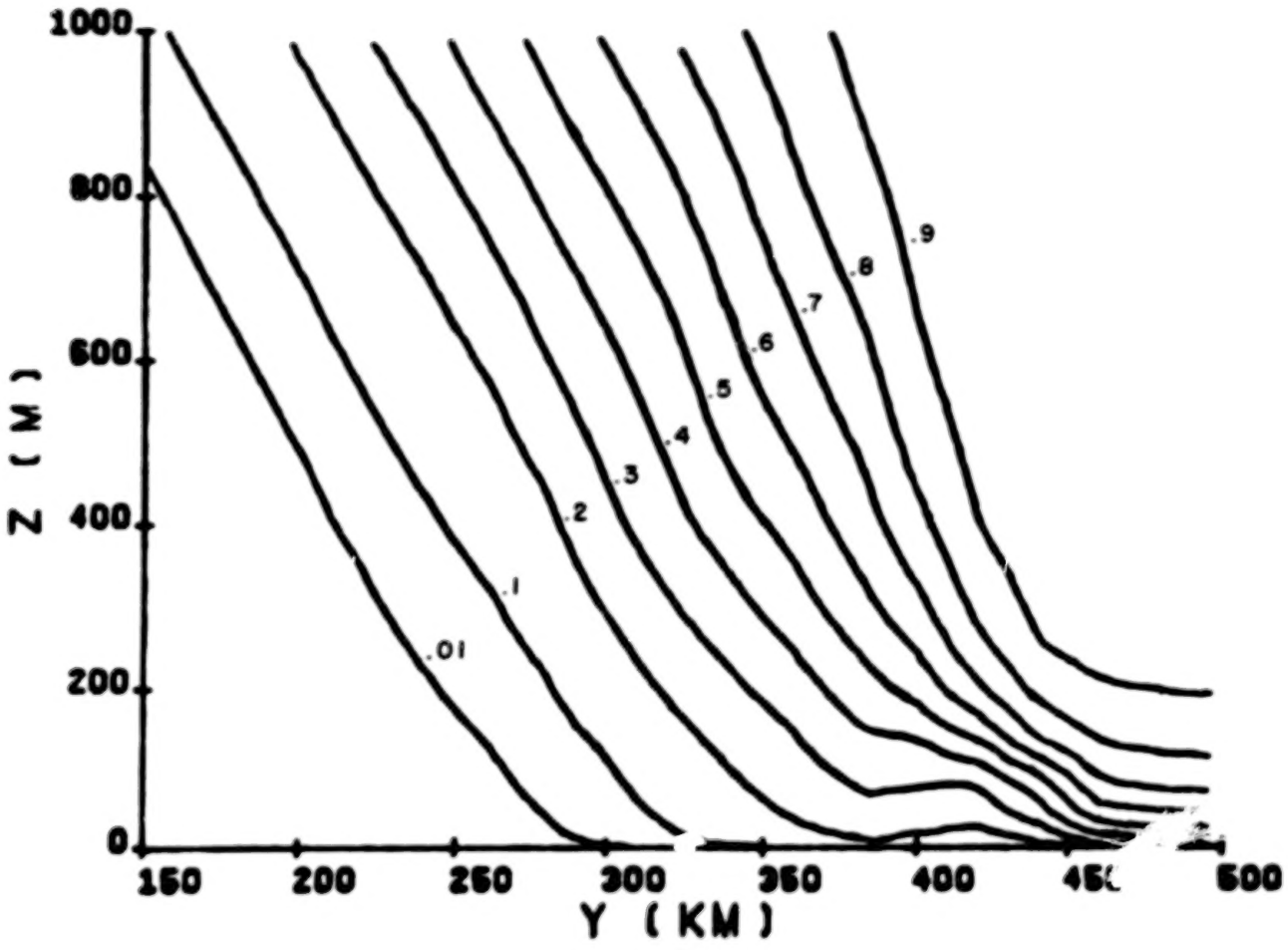

Figure 31. Distribution of potential temperature through a warm front near the surface for $Ro = 10^8$. Contours normalized by total $\Delta\theta$ across the front.

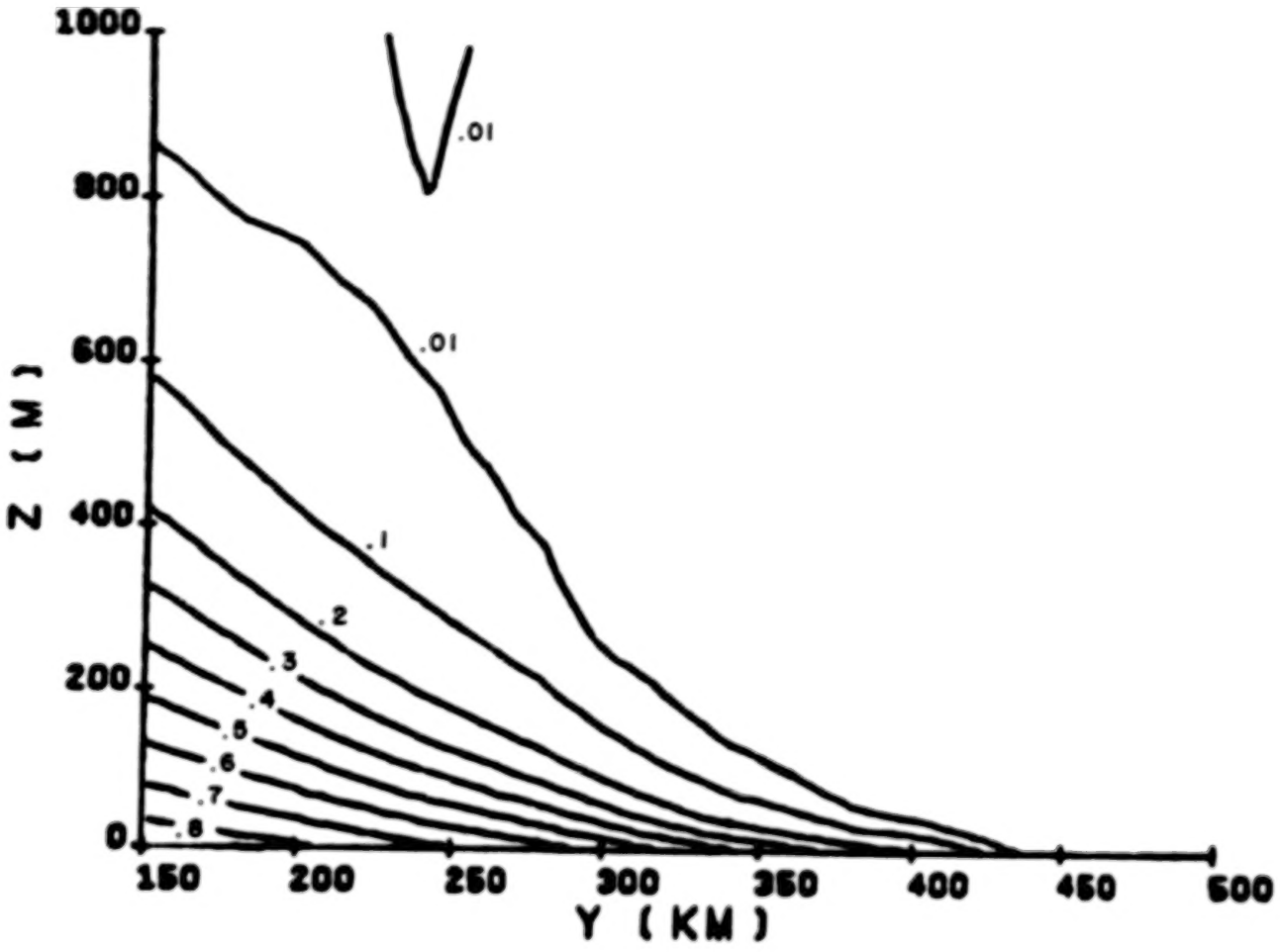

Figure 32. Distribution of the total velocity variance through a warm front near the surface for $Ro = 10^8$. Contours normalized by $q^2_{max} = 0.0056\ (\Delta u_g)^2$.

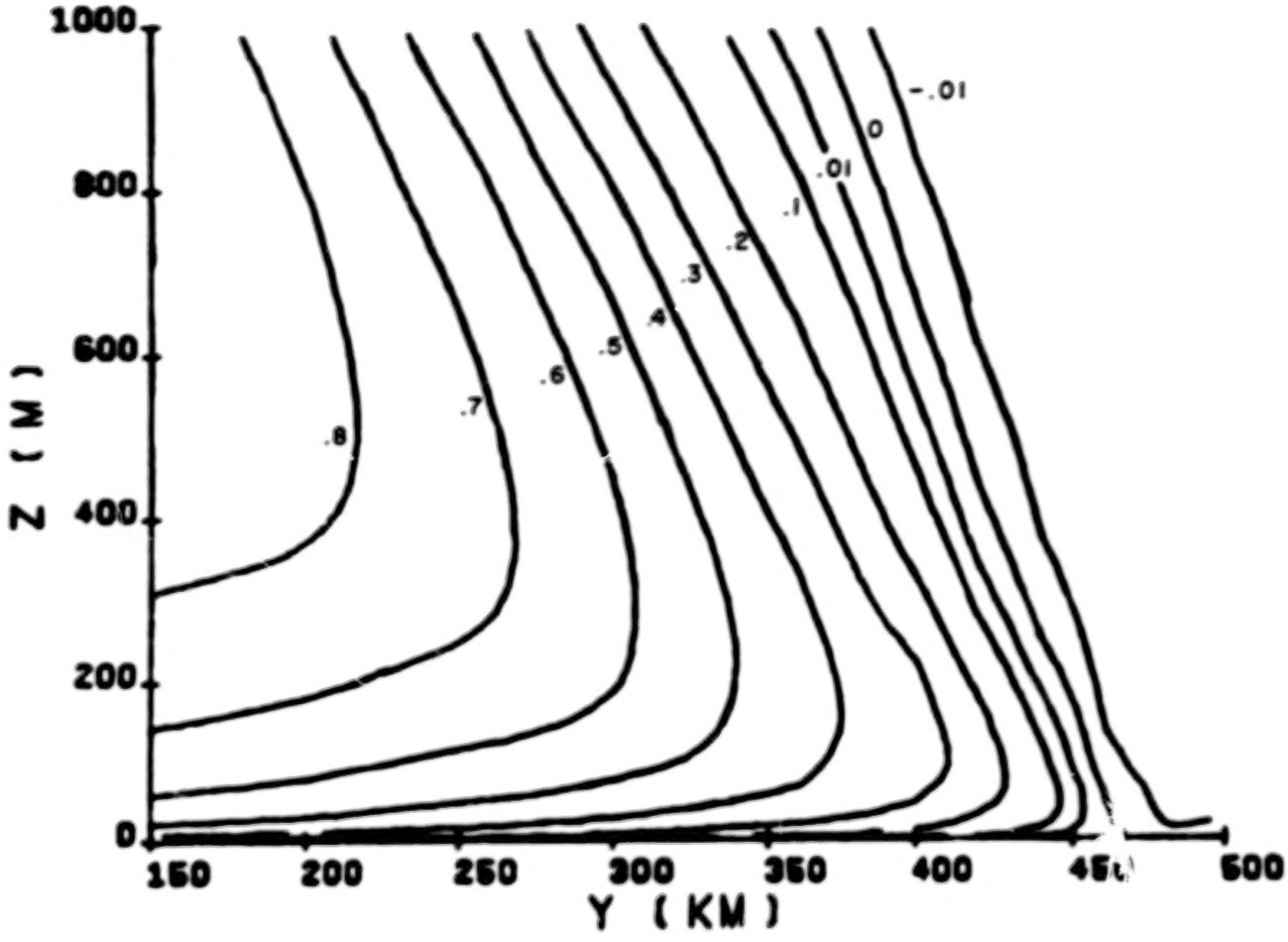

Figure 33. Distribution of mean wind parallel to a warm front near the surface for $Ro = 10^6$. Contours normalized by the total Δu_g across the front.

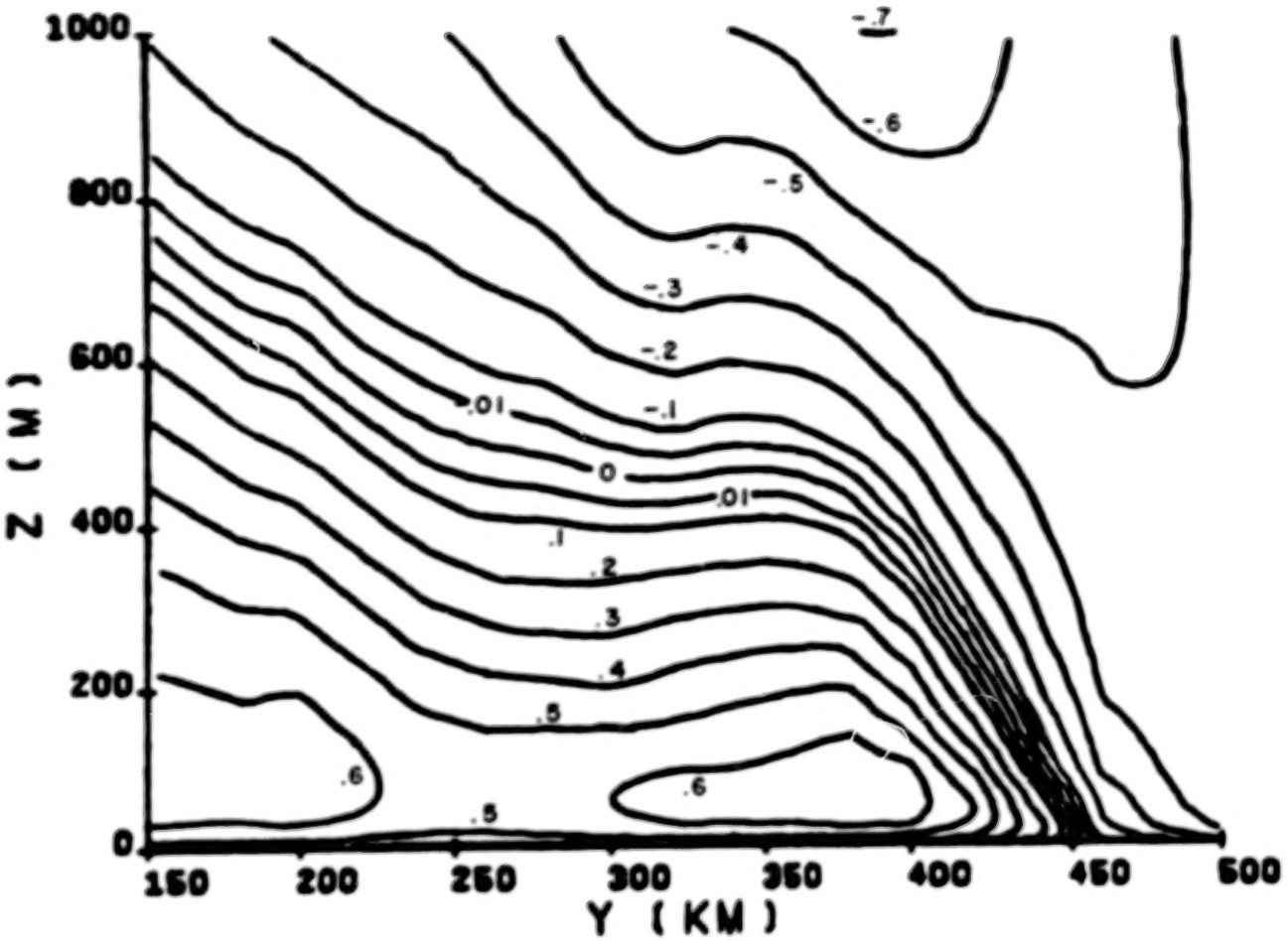

Figure 34. Distribution of mean wind normal to a warm front near the surface for $Ro = 10^6$. Contours normalized by $V_{max} = 0.18\Delta u_g$.

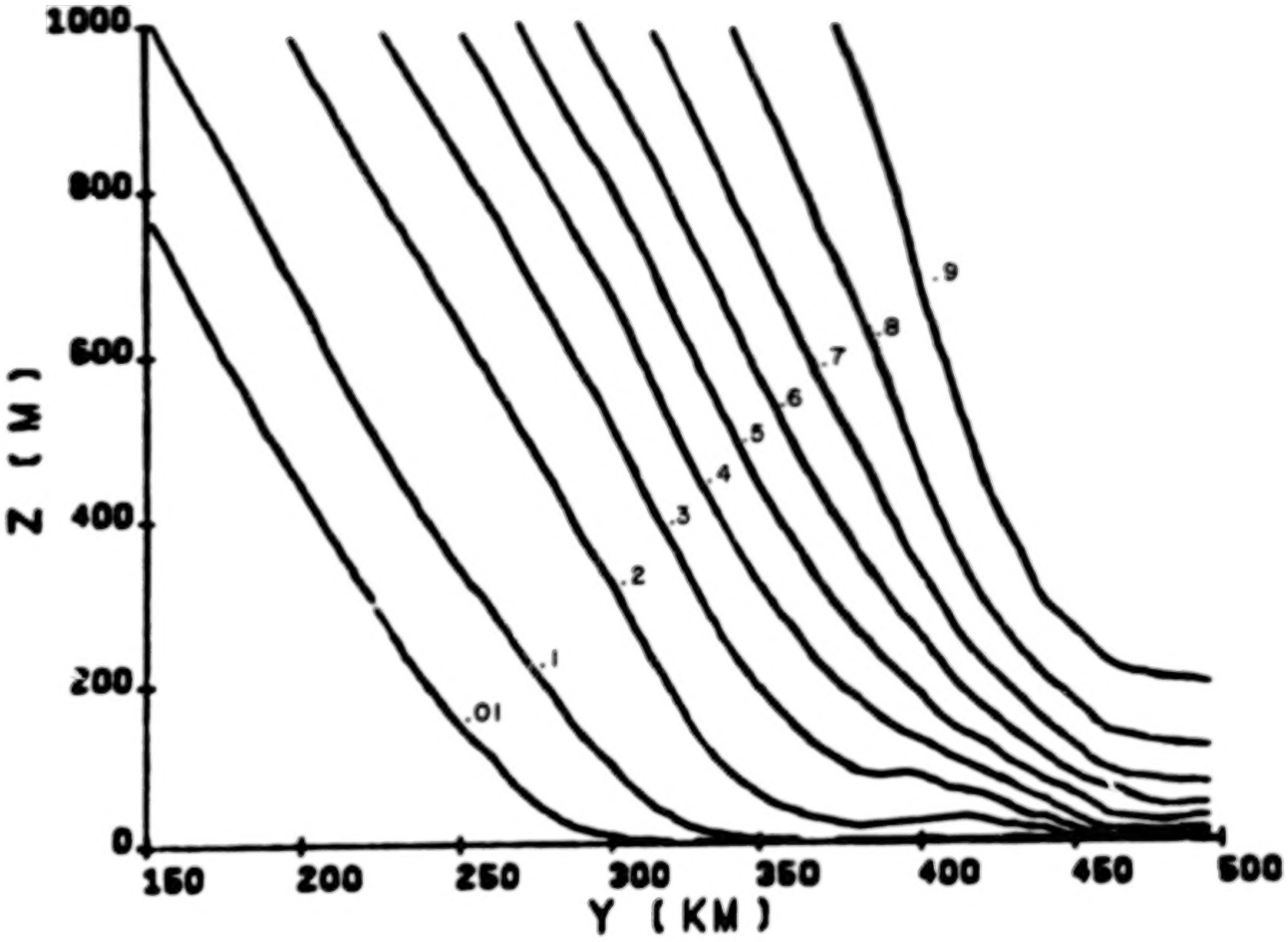

Figure 35. Distribution of potential temperature through a warm front near the surface for $Ro = 10^6$. Contours normalized by total $\Delta\theta$ across the front.

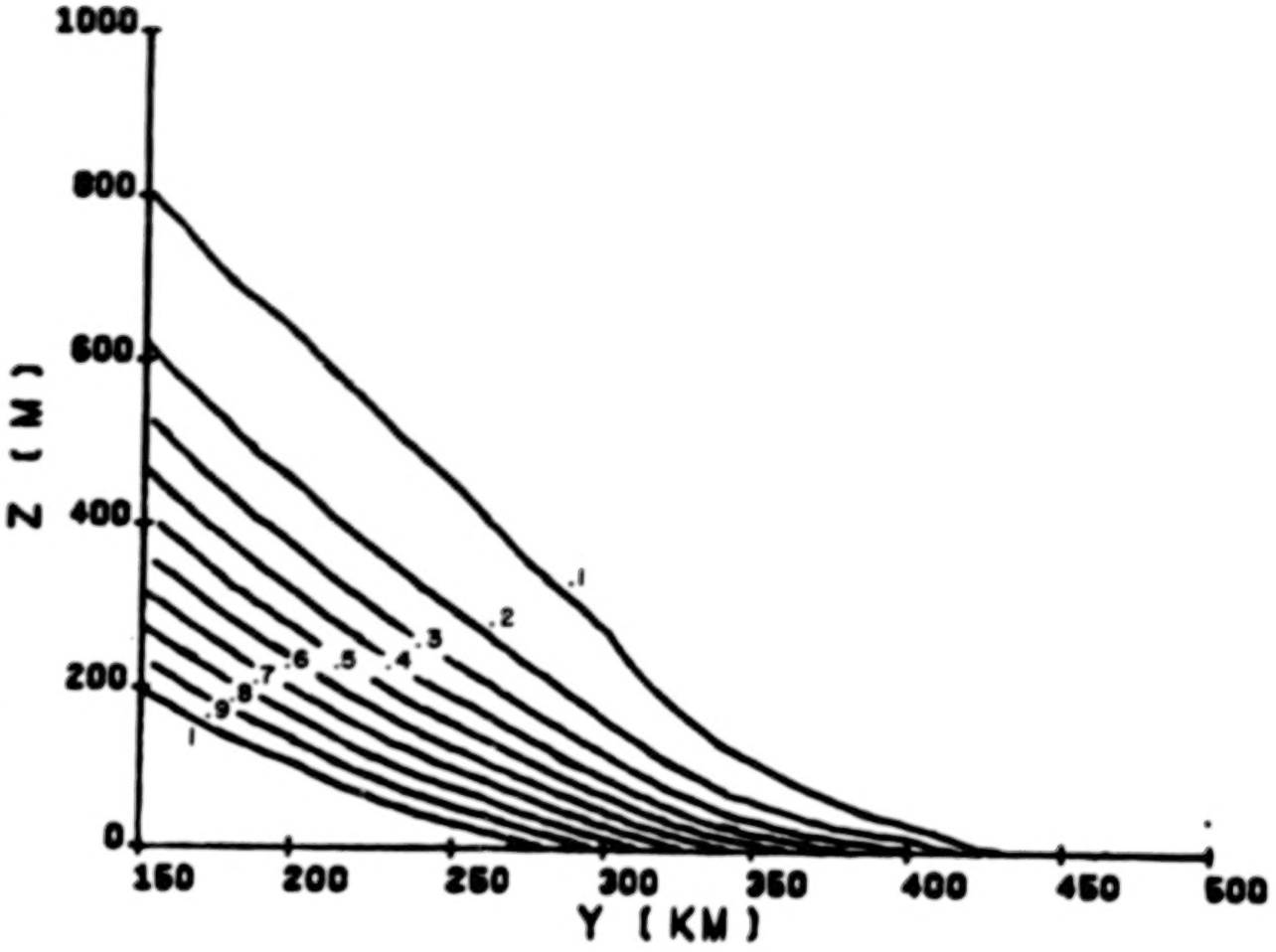

Figure 36. Distribution of the total velocity variance through a warm front near the surface for Ro = 10^3 . Contours normalized by $q^2_{max} = 0.056(\Delta u_g)^2$.

IV. SUMMARY AND RECOMMENDATIONS

Scaling relationships have been given for the wind shear and turbulence existing near the surface in either a thunderstorm gust front or a synoptic scale warm front. Decreasing the surface roughness, increasing the diameter of the downdraft, increasing the potential temperature defect, increasing the height at which the downdraft is released, and increasing the downdraft velocity at the top of the domain all add to the persistence and strength of the gust front.

The gust front was scaled in terms of our simulation model parameters. Further work should be done to relate these model parameters to quantities which are measurable in thunderstorm environments. The quantities $\Delta\theta$, h , σ , w_j are all related to conditions within the parent thunderstorm but are not readily available. Parameters more usually available are those derivable from the prestorm soundings such as the temperature, dew point and wind profiles. The maximum $\Delta\theta$ possible to drive the gust front would be obtained by assuming that mid-tropospheric air is cooled to its dew point by falling rain and then descends along a moist-adiabatic curve to the surface. Estimates based on available prestorm soundings is beyond the scope of the present report.

In the simplified geometry of our model gust front we have not introduced any mean velocity parallel to the gust front. Observations (Ref. 17) often also show significant jumps in this wind component. We believe that our model could also be used to exemplify the role of this wind component in the gust front dynamics. Such a velocity could be particularly important in analyzing the pressure variation associated with the front.

The warm front is shown to be a function of four dimensionless variables. The parameter inducing the strongest influence, Margules' slope parameter, can be incorporated into the scaling of the front structure. Simulation runs were made to determine the influence of Rossby number. Further runs should be made to determine the influence of the two velocity ratios needed to completely specify the geostrophis winds before and after the front.

The wind profiles obtained in the warm front simulations appear to be quite similar to those calculated in Ref. 1 by assuming vertical geostrophic wind gradients. However, the present computation gives us consistent relationships between the vertical temperature gradient and the vertical geostrophic wind gradients. The horizontal thickness of the warm front above 1 km altitude is thicker than anticipated. This introduces the question as to how important change of phase of the water molecule which usually accompanies a strong warm front is to the dynamics of the front. If there is significant change in relative humidity across the front, then it is possible that condensation on the warm side of the front and evaporation on the cold side can act to sharpen the temperature gradient across the front. This is a problem we would like to pursue in the future.

V. REFERENCES

1. Lewellen, W.S.; and Williamson, G.G.: Wind shear and turbulence around airports, Parts 1 and 2. NASA CR-2752, Jan. 1976.

2. Williamson, G.G.; Lewellen, W.S.; and Teske, M.E.: Model predictions of wind and turbulence profiles associated with an ensemble of aircraft accidents. NASA CR-2884, Feb. 1977.

3. Donaldson, C.duP.: Calculation of turbulent shear flows for atmospheric and vortex motions. AIAA Journal, Vol. 10, No. 1, 1972, pp. 4-12. (Dryden Reserach Lecture.)

4. Donaldson, C.duP.: Construction of a dynamic model of the production of atmospheric turbulence and the dispersal of atmospheric pollutants. Workshop on Micrometeorology, American Meteorological Society, Boston, 1973, pp. 313-392.

5. Donaldson, C.duP.: Atmospheric turbulence and the dispersal of atmospheric pollutants. Environmental Protection Agency Report EPA-R4-73-016a, 1973.

6. Lewellen, W.S.; Teske, M.E.; and Donaldson, C.duP.: Turbulence model of diurnal variations in the planetary boundary layer. Proc. 1974 Heat Transfer and Fluid Mechanics Institute (L.R. Davis and R.E. Wilson, eds.), Stanford University Press, 1974, pp. 301-319.

7. Lewellen, W.S.; and Teske, M.E.: Prediction of the Monin-Obukhov similarity functions from an invariant model of turbulence. Journal of Atmospheric Sciences, Vol. 30, No. 7, 1973, pp. 1340-1345.

8. Lewellen, W.S.; Teske, M.E.; and Donaldson, C.duP.: Variable density flows computed by a second-order description of turbulence. AIAA Journal, Vol. 14, No. 3, March 1976, pp. 382-387.

9. Lewellen, W.S.: Use of invariant modeling. Handbook of Turbulence, Vol. 1, Plenum Publishing Corp., 1977, pp. 237-280.

10. Fujita, T.T.: Spearhead echo and downburst near the approach end of a John F. Kennedy airport runway, New York City. SMRP Research Paper 137, The University of Chicago, March 1976.

11. Fujita, T.T.; and Caracena, F.: An analysis of three weather-related aircraft accidents. Bulletin of the American Meteorological Society, Vol. 58, No. 11, Nov. 1977, pp. 1164-1181.

12. Lewellen, W.S.; Williamson, G.G.; and Teske, M.E.: Estimates of the low-level wind shear and turbulence in the vicinity of JFK on the afternoon of 24 June 1975. NASA CR-2751, Oct. 1976.

13. Turner, J.S.; Buoyancy Effects in Fluids. Cambridge University Press, Great Britain, 1973.

14. Lewellen, W.S.; Oliver, D.A.; Teske, M.E.; Segur, H.; and Coté, O.: 1977 Status Report on low-level, atmospheric turbulence model for marine environments. A.R.A.P. Report No. 320 (Prepared for Naval Air Systems Command), Nov. 1977.

15. Bedard, A.J., Jr. Hooke, W.H.; and Beron, D.W.: The Dulles Airport pressure jump detector array for gust front detection. Bulletin of the American Meteorological Society, Vol. 58, 1977, pp. 920-926.

16. Bedard, A.J.; and Cairns, M.M.: Measuring thunderstorm gust fronts using surface sensors. AMS 10th Conference on Severe Local Storms, 1977, pp. 154-159.

17. Palmén, E.; and Newton, C.W.; Atmospheric Circulation Systems. Academic Press, 1969.

18. Goff, R.C.: The thunderstorm-outflow kinematics and dynamics. NOAA TM ERL NSSL-75, 1975.

APPENDIX A

TURBULENT TRANSPORT MODEL OF A THUNDERSTORM GUST FRONT

M. E. Teske and W. S. Lewellen

Aeronautical Research Associates
of Princeton, Inc.
50 Washington Road
Princeton, New Jersey 08540

1. INTRODUCTION

The local gust front created by the rain-cooled outflow from a severe thunderstorm is a familiar phenomenon. The downdraft impinges upon the surface of the earth and spreads radially outward, generating substantial windspeed variation and large windshear near its leading edge and at its core. The developing gust front may extend more than 20 km from the storm (Goff, 1975) and poses a serious hazard to safe aircraft operations. Several accidents over the last few years appear directly attributable to either the downdraft or its accompanying outflow (Williamson, Lewellen, and Teske, 1977).

Probably the most detailed numerical model of this phenomenon previously presented is that by Mitchell (1975). He simulated the gust circulation using a primitive equation model with no direct turbulent transport. Instead, he included several numerical damping mechanisms to suppress any instabilities inherent in his solution approach. Although his results are in qualitative agreement with observations, we believe the problem warrants the use of a consistent turbulent transport model.

An invariant model of turbulence has been under development for several years at A.R.A.P., with work summarized in an early report by Donaldson (1973) and more recent papers by Lewellen (1977) and Lewellen, Teske, and Donaldson (1976). The second paper (by Lewellen) details the extensive model constant determination for incompressible, Boussinesq flows, the development of a dynamic scale equation, and the similarities of our approach with the work of other investigators. In recent work we have simulated complicated flow problems within thermal plumes (Teske and Lewellen, 1976), coastal boundary layers (Lewellen and Teske, 1976), and multiply-shed aircraft vortices (Bilanin, Teske, and Williamson, 1977). In this paper we consider the flow structure around an idealized cold outflow from a thunderstorm.

2. THE MODELED EQUATIONS

The equations for vorticity η, streamfunction ψ, potential temperature θ, and the second-order turbulent correlations needed to close the set are given in Appendix A in an axisymmetric coordinate system. A derivation of the Reynolds equations for the second-order turbulent correlations, and a discussion of the model development and constant evaluation, may be found in Lewellen (1977). Several variables are normalized by r to insure analyticity at $r = 0$. These variables are denoted by the over-tilde $\sim$.

The differential equations are written in finite-difference form on a nonuniformly-spaced grid and solved with a centered-space, forward-time alternating-direction-implicit algorithm. The Poisson equation is evaluated using a fast direct elliptic solver developed by Swarztrauber and Sweet (1975).

3. PROBLEM DEFINITION AND INITIALIZATION

The simulated flowfield is illustrated in Figure 1. We idealize the outflow from the thunderstorm as a cold jet of temperature $\theta_d(r)$ impinging normal to the ground, released at a height z_{max} with vertical velocity $W_d(r)$. The temperature defect below the ambient temperature is caused by evaporation of falling rain by relatively dry air at some altitude $z > z_{max}$. For our simulation we set $\theta_{d_{max}} = -10°C$, with the velocity of the cold jet set to the somewhat arbitrary maximum value of -10 m/sec. Both W_d and θ_d are assumed to have Gaussian distributions with a radial spread of 2 km. The height of the simulation domain is set at $z_{max} = 1600$ m. The cold downdraft

Presented at 10th Conf. on Severe Local Storms, Oct. 18-21, 1977, Omaha, NE.

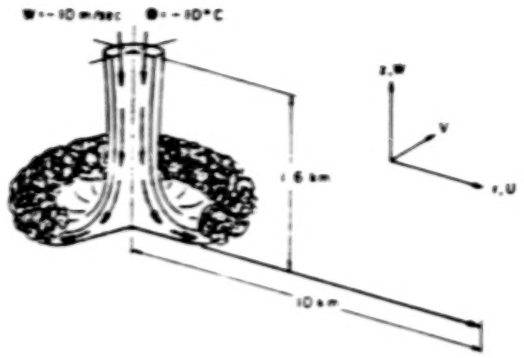

Fig. 1. Coordinate system for the axisymmetric radial thunderstorm gust front simulation.

is opposed by a weakly-convergent flow with an assumed inflow velocity of -2.5 m/sec at the maximum radius, r_{max} = 10 km .

The surface temperature is set equal to the constant ambient potential temperature. This forces the surface layer under the gust to be unstable. However, we expect the Monin-Obukhov length to be sufficiently large, so that the neutral form of the surface layer is adequate for the mean variable relationships at a reference height (z_r = 10 m) where the surface layer boundary conditions are applied. All turbulent correlations are assumed to follow a zero-slope condition at z_r and z_{max} , and be isotropic and small along r_{max} where the inflow is uniform. Surface roughness z_o is set equal to 0.1 m . The scale A is assumed to have an initial value of 0.65 z or 100 m , whichever is smaller.

The streamfunction variation is specified at r_{max} and z_{max} consistent with the ambient convergence and the central downdraft previously described. The vorticity and temperature are prescribed at inflow boundaries and given zero slope at outflow boundaries. At r_{max} both the vorticity and potential temperature defect are set equal to zero.

The primary variables in this simulation are the temperature defect (below ambient) of the jet, its diameter, and the height at which it is released. The larger scale updraft within which the downdraft is embedded will play a role in retarding the late-time gust front within the computational domain, but should not be a critical factor as long as the inflow velocity is smaller than the resulting internal simulated velocities. The other critical parameters are the surface temperature and the surface roughness.

The flow problem is initialized by taking the boundary values of vorticity and temperature at z_{max} and extrapolating them linearly to zero values at the surface. The turbulence is initialized as isotropic. The maximum initial value of q_{max} = 3 m/sec is sufficiently small that it is quickly dominated by turbulent production. The simulation is run for 1200 seconds after initialization, at which time the leading edge of the gust front extends approximately 8 km from the center of the downdraft.

4. SIMULATION RESULTS

A good way to follow the structure of the developing gust is to observe the movement of a fixed temperature value line, in this case θ = -2°C as shown in Figure 2. At t = 0 the initial linear

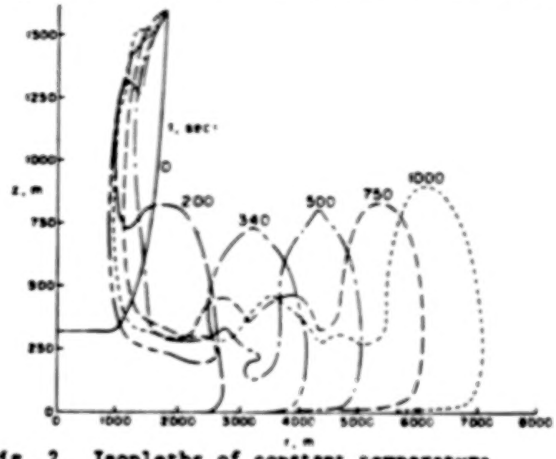

Fig. 2. Isopleths of constant temperature defect (θ = -2°C) at several times after initialization.

profile is shown, but by t = 200 sec the structure has developed into a moving front. At t = 340 sec the front has torn away from the downdraft region. At later times the strength of the gust decreases as the effect of the area change becomes more important. However, the height of the gust appears to grow slowly, so that by t = 1000 sec the θ = -2°C line reaches nearly 1 km in altitude at a distance of nearly 8 km from the souree centerline. The front is still quite strong at this point, and is moving outward at approximately 2.6 m/sec. A sequence of overprint intensity cross-sectional profiles for θ is shown in Figure 3. This sequence shows the initial dropping of the cooler temperature (at t = 100 sec); the formation of the frontal cross-sections (at t = 200 sec); the tearing of the front from the core (by t = 400 sec); the development of waves on the temperature interface (by t = 720 sec); and the establishment of a fairly steady temperature structure at late times for the front and central core regions.

Accompanying cross-sectional contour plots for the radial velocity U and vertical velocity W are shown in Figures 4 and 5. The U velocity shows the development of a line of demarcation between the flow away from and toward the axis at an altitude between 600 m and 1 km.

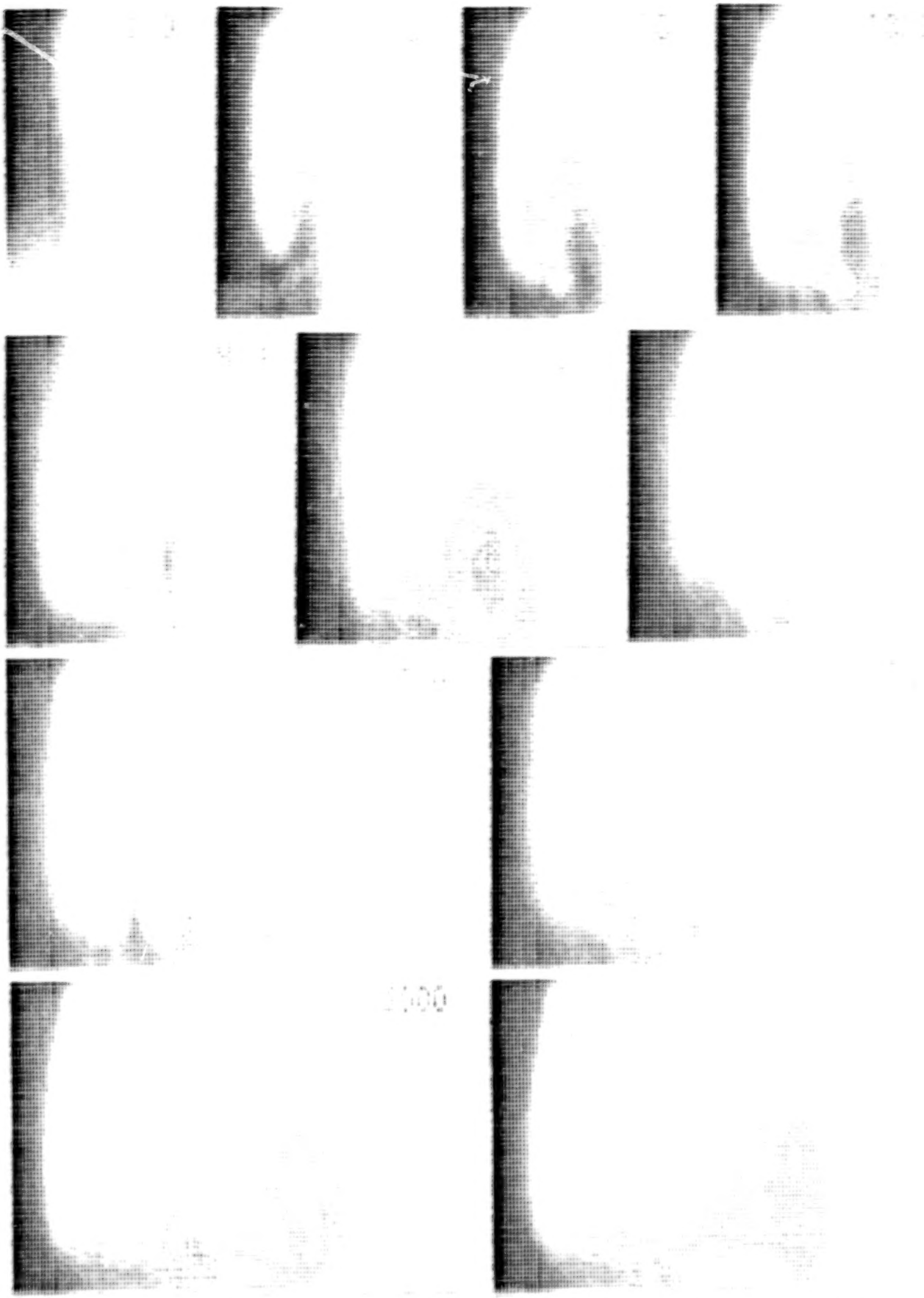

Fig. 3. Overprint intensity cross-sectional profiles for the time-history temperature within the gust front simulation. The darkest areas correspond to the maximum temperature defect of $\theta = -10^{\circ}C$ while the minus sign (-) corresponds to $-1.82^{\circ}C \leq \theta \leq -0.73^{\circ}C$. The horizontal scale is in 1 km increments; the vertical, 160 m increments. Time is given on the figure in seconds.

This line shows the hump over the gust front, the increased radial velocities within the front regions and the increased velocities at altitude in the inflow to conserve mass along cylinders of constant r . The U velocity rapidly reaches a maximum of about 25 m/sec near the surface and remains relatively constant. The W profiles show the development of distinctive up and downdrafts across the front region. A most interesting feature is the location of maximum W , within the central core between 600 and 900 m . Although we are forcing an inflow of 10 m/sec, the simulation determines a maximum downdraft jet of over 18 m/sec in the core.

The computed wind fields are in qualitative agreement with the observations of Goff (1975,1976). The maximum horizontal velocity and maximum updraft

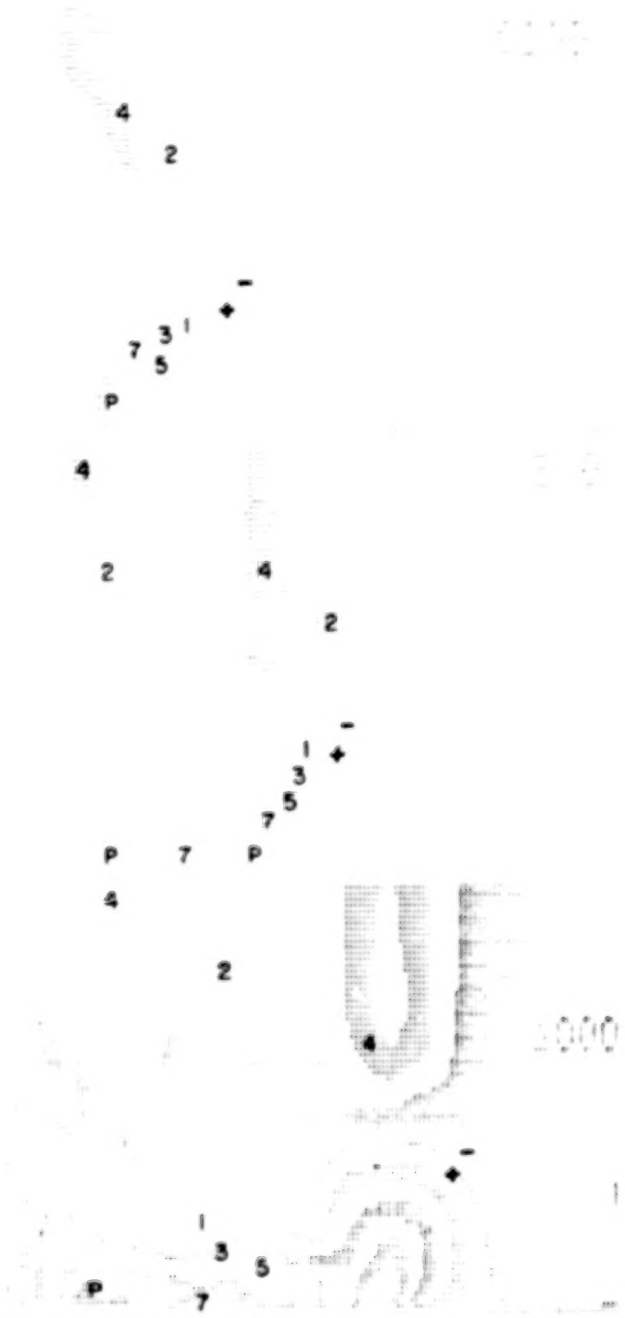

Fig. 4. Contour plots for the radial velocity U at several times after flow initialization. Normalization is by a maximum velocity of 25 m/sec. The figure notation is in percent of maximum; thus, P = 90 to 100%; 7 = 70 to 80%, 5 = 50 to 60%; 3 = 30 to 40%; 1 = 10 to 20%; + = 1%; - = -1%; 2 = -10 to -20%; 4 = -30 to -40%; 6 = -50 to -60%; 8 = -70 to -80%; M = -90 to -100%. The horizontal scale increment is 1 km; the vertical scale 160 m .

Fig. 5. Contour plots for the vertical velocity W at several times after flow initialization. Normalization is by a maximum velocity of 25 m/sec. Figure notation is described in Fig. 4.

velocity are close to those usually observed. Our model result does give a more sharply defined, intense downdraft than Goff usually observed with his top vertical velocity sensor at 444 m . However, he does report (Goff, 1976) the occurrence of a downdraft in excess of -11 m/sec at the 177 m level. So our maximum mean value of ≈-9 m/sec at this level appears reasonable.

A straight tradeoff between potential energy and kinetic energy suggests that the maximum winds in the gust front will vary roughly as the square root of the product of the temperature defect and the characteristic height of the region of depressed temperatures:

$$U_{max},\ W_{max} \sim \left(\frac{g}{\theta_o}\,\theta_{d_{max}}\,z_{max}\right)^{1/2}$$

This rough scaling agrees surprisingly well for both the maximum velocity of the downdraft and the maximum velocity of the radial outflow. The maximum mean velocity occurs at some altitude before the jet starts to stagnate as it approaches the surface. Thus the height associated with W is less than the corresponding height for U .

The associated contour plots of total velocity variance, q and vertical velocity variance $(\overline{ww})^{1/2}$ are shown in Figures 6 and 7 at $t = 1200$ sec. Here we see a substantial turbulence level with $q_{max} \sim 0.4\ U_{max}$ near the stagnation point of the flow, and a less severe level within the gust itself. The evaluation of an eddy viscosity coefficient formed from $\overline{uw}$ and $\partial U/\partial z$ (Figure 8) shows a substantial cross-sectional change across the computational domain and consequently a measure of the error involved in using a constant eddy coefficient. The strong damping of the turbulence at the interface between the cold outflow and the ambient air forces the marked reduction in eddy viscosity and permits the development of strong wind shear.

Fig. 6. Contour plot of the total velocity variance q at $t = 1200$ sec. Normalization is by the maximum root-mean-square velocity of 10.2 m/sec. Notation is described in Fig. 4.

Fig. 7. Contour plot of the vertical velocity variance $(\overline{ww})^{\frac{1}{2}}$ at $t = 1200$ sec. Normalization is by the maximum-root-mean square velocity of 8.5 m/sec. Notation is described in Fig. 4.

Fig. 8. Contour plot of the effective eddy viscosity coefficient $K = -\overline{uw}/(\partial U/\partial z)$ at $t = 1200$ sec. Normalization is by a value of 100 m^2/sec, although the P and M regions contain K values substantially larger. Notation is described in Fig. 4.

The model simulation provides a complete description of the mean wind and turbulence fields from initialization at $t = 0$ sec to $t = 1200$ sec. All of the developing cross-sectional profiles for Ψ, U, W, η, θ, A, $\overline{uw}$, $\overline{u\theta}$, $\overline{w\theta}$, $\overline{\theta^2}$, $\overline{uu}$, $\overline{vv}$, and $\overline{ww}$ have been stored on tape and are available to interested users for a nominal copying fee.

To understand some of the basic variability of the gust simulation, we performed two further gust front calculations. In the first we set the inflow spread of the W velocity equal to 500 m , while in the second, we ran the 2 km case in a Cartesian coordinate system (thereby simulating a squall-line). The cross-sectional profiles are all qualitatively similar to the results shown here. Figures 9 and 10 show the profiles for U and W in the 500 m radial case.

When the spread of the downdraft jet is reduced by a factor of 4, the maximum U and W velocities remain essentially unchanged in the core region but are substantially reduced at the front, as can be seen by comparison with corresponding frames in Figures 4 and 5. The line of demarcation between outflow and inflow U velocity drops from about 600 m to 300 m , with the gust spreading only about 5 km . The increased shear in the central shaft doubles the turbulent kinetic energy there.

In the Cartesian case the squall-line does not have an area change to affect it; consequently the simulation indicates that the gust front is stronger and moves more rapidly than its axisymmetric counterpart. The maximum U near the surface reaches 24 m/sec and W_{max} = 18 m/sec in the core. The turbulence in the core is nearly double the turbulence near r = 0 in the radial gust. The two-dimensional geometry allows the gust front to spread to about 10 km at t = 1000 sec, with a frontal speed of about 7.5 m/sec, nearly three times its axisymmetric value. The line along which U changes sign rises to about 1200 m .

The simple potential and kinetic energy balance indicates that the simulation height z_{max} and maximum temperature defect $\theta_{d_{max}}$ are critical parameters in determining the maximum speeds within the downdraft shaft and the radial front. Even a factor of two increase in both these parameters would probably not lead to a substantial change in the qualitative character of the results presented here. With a stronger convergent flow, the gust front would probably move outward at a slower rate; however, the velocity patterns within the front should again remain faithful to the simulation presented here.

The temperature profiles show a slight curvature at the leading edge. This effect, as well as the scrubbing of the winds along the surface, depends intimately on the difference between the surface and ambient temperatures, and the surface roughness. One would expect that increased surface roughness would accentuate the appearance of the leading edge as the fluid close to the surface is more restricted than the fluid above it. The height and shape of the front region also should be a function of the ambient stability of the atmosphere.

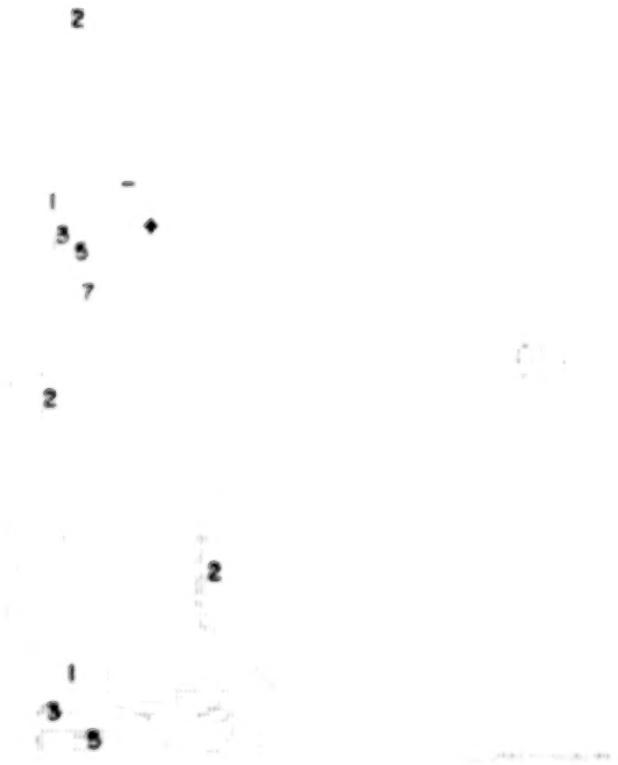

Fig. 9. Contour plots of the radial velocity U at two times after flow initialization with a downdraft spread of 500 m . Normalization is by 25 m/sec; notation is described in Fig. 4.

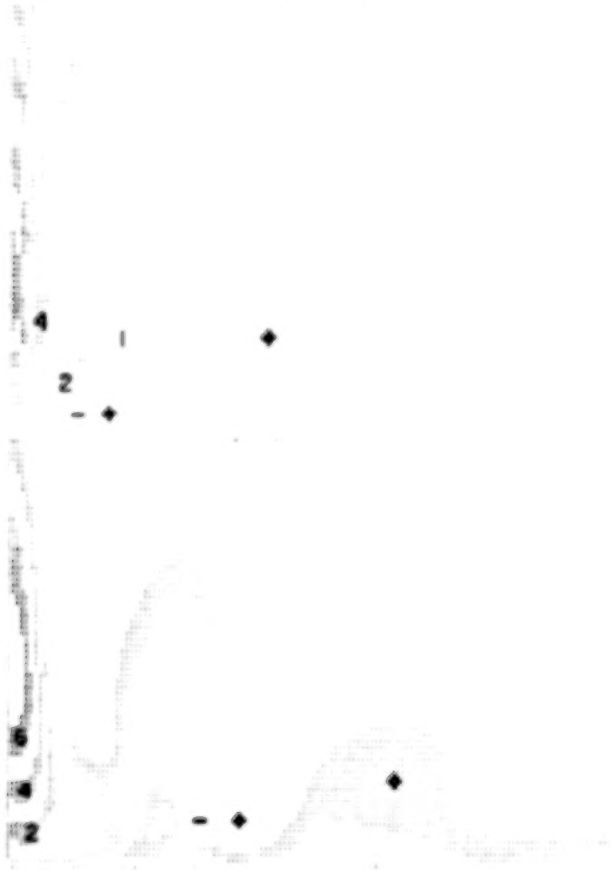

Fig. 10. Contour plots of the vertical velocity W at two times after flow initialization with a downdraft spread of 500 m . Normalization is by 25 m/sec; notation is described in Fig. 4

5. CONCLUDING REMARKS

This simulation demonstrates the relative ease with which a second-order closure turbulent model may be used to predict a decidedly complex fluid flow problem with only a minimum of essential assumptions on appropriate boundary conditions. The evaluation of the modeling constants, the burden of which falls on much simpler flow problems, has permitted the application of the model to flow situations where very few assumptions must be made, a priori, about the internal turbulent and mean flow structure.

With the wind distribution and turbulence modeled, it is possible to predict the environment an aircraft might encounter while flying any assumed trajectory through the flowfield. This has been done by Williamson, Lewellen, and Teske (1977) in an attempt to simulate the environment present at the time of three different thunderstorm-related accidents occurring at Denver on Aug. 7, 1975, Chattanooga on Nov. 27, 1973, and St. Louis on July 23, 1973. The aircraft accident which occurred at JFK airport on June 24, 1975 also appeared to involve flying directly through an intense downdraft cell on final approach (Fujita, 1976 and Lewellen, Williamson, and Teske, 1976) but it was further complicated by the presence of a sea-breeze front.

If an aircraft were flown through the center of downdraft at an altitude of a few hundred meters, it would lose 30-40 m/sec airspeed in a few kilometers as seen in Figure 4. This, even without the accompanying downdraft, produces an extremely hazardous situation for an aircraft flying ≈20 m/sec above its stall speed. Conditions within the gust front are not quite as extreme but are more difficult to anticipate because they occur so far from the storm center. We expect to do a sensitivity analysis on our model to determine which outflow parameters lead to the worst gust front wind shear conditions.

ACKNOWLEDGMENTS

The development of the axisymmetric model was supported by the Nuclear Regulatory Commission under Contract No. AT(49-24)-0218 with R.F. Abbey as technical monitor; and the application to a gust front by the National Aeronautics and Space Administration under Contract No. NAS8-32037 with D. Camp as technical monitor.

REFERENCES

Bilanin, A.J., M.E. Teske, and G.G. Williamson, 1977: Vortex Interactions and decay in aircraft wakes. *AIAA Journal*, 15, 250-260.

Donaldson, C.duP., 1973: Atmospheric turbulence and the dispersal of atmospheric pollutants. *Proceedings of the Workshop on Micrometeorology* (D.A. Haugen, ed.). Amer. Meteor. Soc., Science Press, 313-390.

Fujita, T.T., 1976: Spearhead echo and downburst near the approach end of a John F. Kennedy Airport runway, New York City, SMRP Research Paper 137.

Goff, R.C., 1975: Thunderstorm-outflow kinematics and dynamics. NOAA Tech. Memo. ERL-NSSL, No. 75.

Goff, R.C., 1976: Some observations of thunderstorm induced low-level wind variations. AIAA 9th Fluid and Plasma Dynamics Conference, No. 76-388.

Lewellen, W.S., 1977: Use of invariant modeling. *Handbook of Turbulence*, Plenum Publishers, 237-280; see also Lewellen, W.S., and M.E. Teske, 1976: Turbulence modeling and its application to atmospheric diffusion. EPA-600/4-75-016b.

Lewellen, W.S., and M.E. Teske, 1976: A second-order closure model of turbulent transport in the coastal planetary boundary layer. AMS Conference on Coastal Meteorology, 118-123.

Lewellen, W.S., M.E. Teske, and C.duP. Donaldson, 1976: Variable density flows computed by a second-order closure description of turbulence. *AIAA Journal*, 14, 382-387.

Lewellen, W.S., G.G. Williamson, and M.E. Teske, 1976: Estimates of the low-level wind shear and turbulence in the vicinity of Kennedy International Airport on June 24, 1975, NASA CR-2751.

Mitchell, K.E., 1975: A numerical investigation of severe thunderstorm gust fronts. NASA CR-2635.

Swarztrauber, P., and R. Sweet, 1975: Efficient Fortran subprograms for the solution of elliptic partial differential equations. NCAR-TN/IA-109.

Teske, M.E., and W.S. Lewellen, 1976: Example calculations of atmospheric dispersion using second-order closure modeling. AMS 3rd Symposium on Atmospheric Turbulence, Diffusion and Air Quality, 149-154.

Williamson, G.G., W.S. Lewellen, and M.E. Teske, 1977: Model predictions of wind and turbulence profiles associated with an ensemble of aircraft accidents. (To be published as a NASA CR.)

APPENDIX A.

The modeled axisymmetric equations of motion for the mean variables (denoted by capitals) and the turbulent correlations (lower-case) may be written in the coordinate system shown in Figure 1 as follows:

$$\frac{DP}{Dt} = -\frac{1}{r}\frac{g}{\theta_o}\frac{\partial\theta}{\partial r} - \frac{1}{r}\frac{\partial}{\partial r}\left\{\frac{\partial\overline{uu}}{\partial z} - \frac{1}{r}\frac{\partial}{\partial r}\left(r^2\widetilde{uw}\right)\right\} - \frac{\partial}{\partial z}\left\{\frac{\partial\widetilde{uw}}{\partial z} - \frac{1}{r}\frac{\partial\overline{vw}}{\partial r} + \frac{1}{r^2}\left(\overline{uu}-\overline{vv}\right)\right\}$$

$$\frac{D\theta}{Dt} = -\frac{1}{r}\frac{\partial}{\partial r}\left(r^2\widetilde{u\theta}\right) - \frac{\partial}{\partial z}\left(\overline{w\theta}\right)$$

$$\frac{D\widetilde{uw}}{Dt} = -\overline{uu}\frac{\partial W}{\partial r} - \overline{vw}\frac{\partial\hat{U}}{\partial z} - \frac{q}{\Lambda}\widetilde{uw} + \frac{g}{\theta_o}\widetilde{u\theta} + L(\widetilde{uw}) + \frac{1}{r}\frac{\partial}{\partial r}\left(v_c q\Lambda\widetilde{uw}\right) + \frac{v_c q\Lambda}{r}\frac{\partial\widetilde{uw}}{\partial r}$$

$$\frac{D\widetilde{u^2}}{Dt} = -\frac{\widetilde{u^2}}{r}\frac{\partial r^2\hat{U}}{\partial r} - \overline{uw}\frac{\partial\hat{U}}{\partial z} - \frac{\overline{uu}}{r}\frac{\partial\theta}{\partial r} - \widetilde{uw}\frac{\partial\theta}{\partial z} - \frac{Aq}{\Lambda}\widetilde{u\theta} + L(\widetilde{u\theta}) + \frac{1}{r}\frac{\partial}{\partial r}\left(v_c q\Lambda\widetilde{u\theta}\right) + \frac{v_c q\Lambda}{r}\frac{\partial\widetilde{u\theta}}{\partial r}$$

$$\frac{D\overline{uw}}{Dt} = -r\widetilde{u\theta}\frac{\partial W}{\partial r} - \overline{w\theta}\frac{\partial W}{\partial z} - r\widetilde{uw}\frac{\partial\Omega}{\partial r} - \overline{ww}\frac{\partial\theta}{\partial z} + \frac{g}{\theta_o}\overline{\theta^2} - \frac{Aq}{\Lambda}\overline{w\theta} + L(\overline{w\theta})$$

$$\frac{D\overline{\theta^2}}{Dt} = -2r\widetilde{u\theta}\frac{\partial\Omega}{\partial r} - 2\overline{w\theta}\frac{\partial\Omega}{\partial z} - \frac{2bsq}{\Lambda}\overline{\theta^2} + L(\overline{\theta^2})$$

$$\frac{D\overline{uu}}{Dt} = -2r\overline{uu}\frac{\partial\hat{U}}{\partial r} - 2r^2\widetilde{uw}\frac{\partial\hat{U}}{\partial z} - 2\overline{uu}\hat{U} - \frac{q}{\Lambda}\left[\overline{uu} - q^2/3\right] - \frac{2bq^3}{3\Lambda} + L(\overline{uu}) - \frac{2}{r^2}v_c q\Lambda(\overline{uu}-\overline{vv})$$

$$\frac{D\overline{vv}}{Dt} = -2\overline{vv}\hat{U} - \frac{q}{\Lambda}\left[\overline{vv} - q^2/3\right] - \frac{2bq^3}{3\Lambda} + L(\overline{vv}) + \frac{2}{r^2}v_c q\Lambda(\overline{uu}-\overline{vv})$$

$$\frac{D\overline{ww}}{Dt} = -2r\widetilde{uw}\frac{\partial W}{\partial r} - 2\overline{ww}\frac{\partial W}{\partial z} - \frac{q}{\Lambda}\left[\overline{ww} - q^2/3\right] - \frac{2bq^3}{3\Lambda} + \frac{2g}{\theta_o}\overline{w\theta} + L(\overline{ww})$$

$$\frac{D\Lambda}{Dt} = -s_1\frac{\Lambda}{q^2}\left[r\overline{uu}\frac{\partial\hat{U}}{\partial r} + r^2\widetilde{uw}\frac{\partial\hat{U}}{\partial z} + (\overline{uu}+\overline{vv})\hat{U} + r\widetilde{uw}\frac{\partial W}{\partial r} + \overline{ww}\frac{\partial W}{\partial z}\right] - s_2 bq + L(\Lambda) - \frac{s_3}{q}\left[\left(\frac{\partial q\Lambda}{\partial r}\right)^2 + \left(\frac{\partial q\Lambda}{\partial z}\right)^2\right] + s_4\frac{\Lambda}{q^2}\frac{g}{\theta_o}\overline{w\theta}$$

where

$$q^2 = \overline{uu} + \overline{vv} + \overline{ww}$$

$$\frac{D(\ )}{Dt} = \frac{\partial(\ )}{\partial t} + \frac{1}{r}\frac{\partial}{\partial r}\left(r^2\hat{U}(\ )\right) + \frac{\partial}{\partial z}\left(W(\ )\right)$$

$$L(\ ) = \frac{1}{r}\frac{\partial}{\partial r}\left(rv_c q\Lambda\frac{\partial(\ )}{\partial r}\right) + \frac{\partial}{\partial z}\left(v_c q\Lambda\frac{\partial(\ )}{\partial z}\right)$$

and $\hat{U}$ and W are found by solving the Poisson equation for the streamfunction ψ

$$\frac{\partial^2\psi}{\partial r^2} - \frac{1}{r}\frac{\partial\psi}{\partial r} + \frac{\partial^2\psi}{\partial z^2} = -r^2\Omega$$

with

$$\hat{U} = -\frac{1}{r^2}\frac{\partial\psi}{\partial z} \qquad W = \frac{1}{r}\frac{\partial\psi}{\partial r}$$

The modeling constants carry the values: $v_c = 0.3$; $A = 0.75$; $b = 0.125$; $s = 1.8$; $s_1 = -0.35$; $s_2 = -0.6$; $s_3 = 0.375$; and $s_4 = 6.8$. The equations include gravity g and surface temperature θ_o .

TECHNICAL REPORT STANDARD TITLE PAGE

1. REPORT NO.	2. GOVERNMENT ACCESSION NO.	3. RECIPIENT'S CATALOG NO.
NASA CR-3002		

4. TITLE AND SUBTITLE	5. REPORT DATE
Turbulent Transport Model of Wind Shear in Thunderstorm Gust Fronts and Warm Fronts	May 1978
	6. PERFORMING ORGANIZATION CODE

7. AUTHOR(S)	8. PERFORMING ORGANIZATION REPORT #
W. S. Lewellen, M. E. Teske, and H. Segur	A. R. A. P. Report No. 327

9. PERFORMING ORGANIZATION NAME AND ADDRESS	10. WORK UNIT NO.
Aeronautical Research Associates of Princeton, Inc. 50 Washington Road, P. O. Box 2229 Princeton, New Jersey 08540	M-253
	11. CONTRACT OR GRANT NO.
	NAS8-32037
	13. TYPE OF REPORT & PERIOD COVERED
	Contractor

12. SPONSORING AGENCY NAME AND ADDRESS	14. SPONSORING AGENCY CODE
National Aeronautics and Space Administration Washington, D. C. 20546	

15. SUPPLEMENTARY NOTES

This report was prepared under the technical monitorship of the Atmospheric Sciences Division, Space Sciences Laboratory, Marshall Space Flight Center, Huntsville, Alabama.

16. ABSTRACT

The Aeronautical Research Associates of Princeton, Inc. (A. R. A. P.) model of turbulent flow in the atmospheric boundary layer is used to simulate the low-level wind and turbulence profiles associated with both local thunderstorm gust fronts and synoptic-scale warm fronts. Dimensional analyses of both type fronts provide the physical scaling necessary to permit normalized simulations to represent fronts for any temperature jump. The sensitivity of the thunderstorm gust front to five different dimensionless parameters as well as a change from axisymmetric to planar geometry is examined. The sensitivity of the warm front to variations in the Rossby number is examined. Results of the simulations are discussed in terms of the conditions which lead to wind shears which are likely to be most hazardous for aircraft operations.

17. KEY WORDS	18. DISTRIBUTION STATEMENT
Wind shear Thunderstorm gust front Warm fronts Atmospheric turbulence Turbulence modeling	Category 02

19. SECURITY CLASSIF. (of this report)	20. SECURITY CLASSIF. (of this page)	21. NO. OF PAGES	22. PRICE
Unclassified	Unclassified	67	$5.25

* For sale by the National Technical Information Service, Springfield, Virginia 22161

NASA-Langley, 1978

END

9. 19. 78